1   **Correlative cryogenic montage electron tomography for comprehensive in-situ**

2   **whole-cell structural studies**

3

4   Jie E. Yang[1,2,3], Matthew R. Larson[1,2,3,#], Bryan S. Sibert[1,2,3,#], Joseph Y. Kim[1,4,#], Daniel

5   Parrell[1], Juan C. Sanchez[1,5], Victoria Pappas[1,5], Anil Kumar[1,2,3], Kai Cai[1,2,3], Keith

6   Thompson[1,2,3], Elizabeth R. Wright[1,2,3,6,*]

7

8   [1]Department of Biochemistry, University of Wisconsin, Madison, WI USA

9   [2]Cryo-Electron Microscopy Research Center, Department of Biochemistry, University of

10 Wisconsin, Madison, WI USA

11 [3]Midwest Center for Cryo-Electron Tomography, Department of Biochemistry, University

12 of Wisconsin, Madison, WI USA

13 [4]Department of Chemistry, University of Wisconsin, Madison, WI USA

14 [5]Biophysics Graduate Program, University of Wisconsin, Madison, WI USA

15 [6]Morgridge Institute for Research, Madison, WI, USA

16 [#]These authors contributed equally

17 *To whom correspondence should be addressed.

18 E-mail: erwright2@wisc.edu; Tel.: (+1) 608-265-0666; Fax: (+1) 608-265-4693

19   **Abstract**

20   **Imaging large fields of view while preserving high-resolution structural information**

21   **remains a challenge in low-dose cryo-electron tomography. Here, we present**

22   **robust tools for montage electron tomography tailored for vitrified specimens. The**

23   **integration of correlative cryo-fluorescence microscopy, focused-ion beam milling,**

24   **and micropatterning produces contextual three-dimensional architecture of cells.**

25   **Montage tilt series may be processed in their entirety or as individual tiles suitable**

26   **for sub-tomogram averaging, enabling efficient data processing and analysis.**

27

28   **Main**

29   There is an increasing interest and need for a comprehensive understanding of the

30   structure and function of macromolecules, both isolated and within the context of a larger

31   biological system. While cryo-electron microscopy (cryo-EM) of purified proteins (e.g.,

32   single-particle cryo-EM) has propelled the cryo-EM 'resolution resolution'[1], *ex-situ*

33   conditions may not capture cellular interactions taking place between biological molecules

34   in a native context. Cryo-electron tomography (cryo-ET) links three-dimensional (3D)

35   contextual visualization and high-resolution structure determination of cryogenically

36   preserved macromolecular complexes in their native cellular environment[2], unperturbed

37   by purification or chemical fixation and staining[3,4]. Computationally extracted sub-

38   tomograms can be analyzed and classified to reveal sub-nanometer (sub-5 Å) to

39   nanometer (1~3 nm) resolution structures of *in-situ* complexes[5]. Cryo-ET is generally

40   restricted to investigations of small specimen volumes and the thin peripheral areas of

41   cells (< 500 nm) that are penetrable by the electron beam. To explore thicker regions of

42   cells, sample thinning technologies have evolved and include cryo-electron microscopy

43   of vitreous sections (CEMOVIS)[6] and cryo-focused ion beam (cryo-FIB) milling[7]. Both

44   methods produce thin sections or lamella from bulk materials, but each may be impacted

45   by preparative artifacts such as sample compression or curtaining, respectively. Cryo-

46   correlative light and electron microscopy (cryo-CLEM)[8] correlates the temporal and

47   spatial information from fluorescence light microscopy (FLM), with ultrastructural data

48   from cryo-ET of the same region of interest (ROI) while retaining context. In combination

49   with cryo-FIB milling, it is now possible to pinpoint an area of interest deep in the interior

50   of a specimen through 3D correlative cryo-FLM-FIB-ET[9]. However, it remains challenging

51   to bridge the disparity of the spatial scales in multi-modal microscopy pipelines where the

52   field of view (FOV) in wide-field FLM can be 10^5 times (~0.1 to 5 mm) that of an EM FOV

53   (~200 nm to 800 μm)[2,10].

54

55   In cryo-ET, tilt series acquisition of an ROI involves tilting the cryo-preserved specimen

56   along one or two axes[11] while a series of projection images is incrementally captured on

57   a detector. Tilt series of the same region could be collected at both high and low

58   magnifications for subsequent reconstruction into 3D tomograms to obtain high-resolution

59   structural information[12] and overall landscape visualization, respectively. However, this

60   could be difficult to implement due to the radiation sensitivity of frozen-hydrated biological

61   materials and the need to use low-dose exposure routines (~1-3 e$^-$/Å^2/tilt) that must

62   maintain sufficient signal over background noise at each tilted image to support individual

63   frame, image, and tilt series alignment. Advances in detector design have supported the

64   use of larger format detectors for certain applications[13]. Of note, detector size scales

65 exponentially with the volume of the data being digitized, thus imposing challenges to

66 hardware and software infrastructure[14]. These technical hurdles and others[5] have

67 constrained the application of cryo-ET to fractional volumes of cells that result in

68 significant losses to the FOV and contextual information. An approach for obtaining 3D

69 tomograms that encompass a larger FOV is to collect montages of tilt series. The

70 development of montage cryo-ET has been limited. To our knowledge, only one method[15]

71 has been reported. As noted by the authors, major challenges included seamlessly joining

72 cryo-EM montage tiles with improved automation[15], processing large volume stitched

73 tomograms[16], and sub-tomogram averaging (STA).

74

75 Here, we demonstrate our adaptation of the principles of montage tomography, which

76 is routinely applied to resin-embedded samples[17,18], to frozen-hydrated specimens via

77 montage cryo-ET. This montage cryo-ET data collection routine and automated

78 processing schemes (Supplementary Fig. 1) are robust solutions for the generation of

79 molecular-level resolution 3D reconstructions of vitrified specimens.

80

81 We employed image-shift montage acquisition[17,19] to acquire overlapping tiles of

82 defined size at each tilt increment. Rectangular or square montage tile patterns and tile

83 overlaps were investigated while considering: 1) Fresnel fringes formed inside the image

84 detector FOV from the C2 aperture of an electron microscope[20] introduce non-uniform

85 illumination and disruption in image signals (Supplementary Fig. 2a). Under a

86 magnification (4.6 Å /pixel) and defocus value (-5 μm) typical for cryo-ET collection, the

87 beam fringe artifact was determined to affect up to 3 to 4% of the FOV extending from the

88   outer edge of the 3.11 μm illuminated area (Supplementary Fig. 2b) when the outer edge

89   of the beam intersected the camera at ~4% of its long axis. 2) Under parallel illumination,

90   the beam size relative to the camera frame determines the captured FOV and fringe-

91   unimpacted or 'fringeless' area (Supplementary Fig. 2c-d). The FOV affected by Fresnel

92   fringes becomes increasingly evident as the beam size decreases under a constant

93   magnification and defocus (Supplementary Fig. 2d-e). Yet, use of an expanded beam and

94   larger illuminated areas to minimizing in-frame fringes also impacts the sample through

95   excess pre-exposure irradiation (Supplementary Fig. 2c). 3) Robust automation of

96   montage stitching at each tilt requires consistent overlap regions between adjacent tiles.

97   Compared to resin-embedded samples where the image contrast is strong[18], reliable tile

98   overlaps at a majority of the tilts are essential in vitrified unstained samples to achieve

99   gap-free stitching[15]. 4) Sorting of individual tile tilt series from the complete montage

100   collection for efficient data processing and sub-tomogram averaging is applicable only

101   when each tile frame contains enough fringe-unimpacted FOV and retains the ROI

102   throughout the tilt series.

103

104   An inherent limitation of montage cryo-ET is the uneven accumulation of dose in

105   overlapping regions between adjacent tiles, which leads to excessive radiation damage.

106   Therefore, we adopted an additional globally applied translation shift that was calculated

107   from the central tile of a montage pattern (Supplementary Figs. 3, 4, 9a). To quantitatively

108   assess cryo-ET data collection and montage tiling strategies, we developed

109   TomoGrapher, a user-friendly simulation tool to visualize tilt series collection routines and

110   determine global and localized electron dose accumulation (Supplementary Fig. 3).

111 TomoGrapher supports simulation of tilt series acquisition with and without a translational

112 shift extending along spiral paths (Supplementary Fig. 4a-f, Table 1). The shape of the

113 spiral trajectory can be adjusted to vary dose accumulation on each voxel over the full tilt

114 range. Circular beam projections and the associated images gradually elongate to

115 ellipses along the X-axis perpendicular to the tilt axis (Y-axis) as the tilt angle increases

116 (Supplementary Figs. 3b, 4c-d), resulting in stretching of the spiral paths. Optional X-axial

117 correction and cosine-weighting[21] of dose can be implemented in the simulation process

118 (Supplementary Fig. 3). Within the maximum offset distance permitted to retain the FOV

119 in the full tilt range, simulation results suggest larger translations and axial correction

120 introduce more uniformly spread dose (Supplementary Fig. 4g-h).

121

122 Overall, both simulation results and experimental data demonstrate the incorporation

123 of a global translational shift allowed for a more even distribution of the total electron dose

124 across each montage tile and tile overlap regions where accumulated dose would

125 otherwise be much higher (Supplementary Fig. 4, Table 1). We determined that a 15 to

126 20% overlap in X (fringe-affected axis) and 10% in Y (fringe-unaffected axis) of tile frames

127 was sufficient for automated gap-free tile stitching without human intervention at tilt angles

128 up to $\pm 39°$ and minimal manual fixation at higher tilt angles ($\pm$ 40° to 60°) using

129 coordinate-based image cross-correlation[22] (Supplementary Figs. 5a-c). We explored the

130 addition of rotation to translation of the tile montage pattern to further spread the dose.

131 Our data (Supplementary Fig. 5d) support a common observation that rotation of the in-

132 plane image shift deviates significantly from the designated coordinates as the stage tilt

133 increases[23]. This departure in image shift values introduced by global tile rotation was

134   much larger than the applied translation alone at lower tilts and became particularly

135   irregular as the stage was tilted to degrees greater than ±30°. As a result, the inconsistent

136   overlap between tiles caused problematic stitching, consistent with previous reports[15,18].

137

138   We integrated montage cryo-ET with 2D and 3D correlative cryo-CLEM and cryo-FIB

139   routines using CorRelator[24], 3DCT[9], and SerialEM[19] to image large, targeted FOV along

140   the periphery of HeLa cells (Supplementary Fig. 6) and cryo-FIB-milled lamella near the

141   nucleus of adenocarcinomic human alveolar basal epithelial (A549) cells (Fig. 1,

142   Supplementary Fig. 7). Both cell lines are commonly used for studies of both

143   mitochondrial function and respiratory syncytial virus (RSV) infection[25,26]. A pixel size of

144   4.6 Å was used to support the large FOV and STA sampling requirements[12]. 2D cryo-

145   CLEM was applied to identify fields of long, filamentous RSV particles budding from

146   metabolically active RSV-infected HeLa cells[26] for montage cryo-ET data collection

147   (Supplementary Fig. 6). Montage tomograms of RSV particles up to 8 μm in length

148   revealed the ultrastructure of intact virions and organization of viral compartments

149   (Supplementary Fig. 6g). To explore mitochondrial function and organization closer to the

150   nucleus in naïve and RSV-infected A549 cells, we coupled 3D targeted cryo-FLM-FIB-

151   milling with montage cryo-ET (Fig. 1, Supplementary Fig. 7). Low toxicity fluorescent

152   nanoparticles (40 nm)[27] were internalized by the cells and used as FIB-milling "fiducials"

153   to position and adjust milling boxes on-the-fly in the Z and XY planes based on the

154   position of nanoparticles relative to the ROI in the 3D cryo-FLM Z-stack (Supplementary

155   Figs. 7, 8b-c). A square of interest was identified (Fig. 1a) and milling boxes were initially

156   positioned via external markers using 3DCT[9] and CorRelator[24] (Fig. 1b, Supplementary

157 Fig. 8c), then further adjusted based on the FIB-milling "fiducials" (Supplementary Fig.

158 8d-f) during the thinning process. Uniformly-sized nanoparticles can be readily

159 differentiated from electron dense lipid droplets by SEM and cryo-ET (Fig. 1c,

160 Supplementary Fig. 8j-m). Post correlation[28] of cryo-EM images of lamella with the

161 corresponding pre-milling cryo-FLM section confirmed the locations of ROIs and

162 nanoparticles (Fig. 1d-f, Supplementary Fig. 8h-i). We targeted fluorescently-labeled

163 mitochondria-rich areas near the nucleus where multiple 3X3 montage cryo-ET fields

164 were collected; each montage covering an area of ~7 x 5.5 μm (representative 3X3

165 montage tile in cyan box, Fig. 1e). The 3D correlative targeting in combination with

166 montage cryo-ET supported the precise acquisition of large FOVs of a FIB-thinned

167 cellular lamella. Within the 3D volume, the arrangement of mitochondria, the Golgi, rough

168 ER, and nuclear pore complex along the nuclear envelope was observed with potential

169 to retrieve high-resolution structural information[12] (Fig. 1f).

170

171 Next, we applied montage cryo-ET to primary neurons grown on micropatterned cryo-

172 TEM grids[29,30]. Coupling micropatterning with cryo-ET has proven to be valuable for

173 directing cytoskeleton organization and understanding neural outgrowth[30]. Straight-line

174 patterns were used to control neurite growth of primary *Drosophila melanogaster* neurons

175 (Fig. 2a-c). Multiple montage tilt series were collected along neurites protruding from

176 peripheral areas of the cell body (representative 3X4 montage site (~8 x 7 μm) delineated

177 in Fig. 2d). The montage cryo-tomogram revealed the architecture of the cytoskeleton,

178 including continuous microtubules (~9 μm) stretching along the pattern and the presence

179 of actin filaments extending from the neurite. The localization and 3D organization of

180 mitochondria that exhibited matrix regions densely packed with calcium granules was

181 indicative of possible metabolic activities[31] (Fig. 2e-f). The application of cryo-montage

182 tomography is important for generating large-scale 3D molecular vistas of neurons and

183 other cells that are responding to external physical cues such as those imposed by

184 micropatterning.

185

186 A completely reconstructed unbinned tomogram of a fully stitched 3X4 montage tilt

187 series could be ~700 GB or more, particularly as the sampling pixel size decreases and

188 tile pattern size expands. To maximize output and develop efficient processing schemes,

189 we explored sorting individual tile tilt series and independently reconstructing them into

190 tile tomograms that have the same volume and pixel size as a regular single cryo-

191 tomogram. Consistent with simulation results (Supplementary Figs. 4, 5), each tile tilt

192 series exhibited the same spiral image shift trajectory as the fully-stitched montage tilt

193 series (Supplementary Fig. 9a-b). When the largest image translation offset was restricted

194 to 30% or less of the FOV per image, each tile tilt series maintained the specified ROI

195 within the majority of the tilt series images. After determining the eucentric plane of the

196 montage field, per tilt focus and per group tracking were adjusted using the nearby focus

197 area during the dose-symmetric acquisition. CTF determination using CTFPLOTTER[32]

198 indicated that the data acquisition scheme provided a relatively stable defocus ($\pm\,1\,\mu m$)

199 over tilt series acquired from a wide range of samples (Supplementary Fig. 9c). We used

200 CTFFIND4 for tilted defocus determination[23]. CTFFIND4 reported the high-resolution limit

201 of detected Thon rings that ranged from 8 to 20 Å for individual tiles and stitched montages

202 at 0° tilt and high tilts (Supplementary Fig. 9d). Per tile defocus adjustment could be

203   implemented to decrease defocus variation. We performed sub-tomogram averaging on

204   the RSV F fusion (F) glycoprotein to compare with our previous results[33]. Viral F

205   glycoproteins are arrayed on the surface of filamentous RSV particles either budding or

206   released from RSV-infected BEAS-2B cells grown on EM grids (Supplementary Fig. 10a-

207   e). Volumes containing F were extracted from individually-reconstructed tile tomograms

208   for STA (n = 23250, ~29 Å, C3 symmetry imposed). In an effort to determine whether an

209   improved sub-tomogram average would result from the removal of particles located along

210   stitched overlap zones (15% of X and 10% of Y edges), 971 particles from those regions

211   out of the 7947 total unique particles were removed to yield a refined average of F at ~26

212   Å resolution (n = 20707, C3 symmetry imposed). These averaged F structures were on

213   par with what has been reported[33]. We anticipate further improvements to the average

214   could be gained, in part, by using a lower defocus range, a larger number of particles,

215   and further refinement of particles included in the average based upon position in

216   individual tile tomograms.

217

218   In conclusion, correlative cryo-montage tomography is a workflow suited for capturing

219   both comprehensive fields of view and targeted regions of interest in complex biological

220   environments at molecular-level resolution. The montage cryo-ET tools presented here

221   are applicable for modern TEMs with stable lens systems. Montage cryo-ET is adaptable

222   to existing imaging routines and supports flexible user-defined tile patterns, streamlined

223   data acquisition, pre-processing automation, and maximization of cryo-ET output with

224   both individual tile and montage tilt series. Rectangular array tile montage for cryo-ET has

225   laid the foundation for future developments with super-montage tomography that

226   incorporate both image-shift and stage-shift collection[17]. Cryo-ET tilt series are commonly

227   acquired at the highest tolerable dose for the biological target; future work will assess the

228   impact of total dose, dose distribution, and montage tile stitching on the preservation of

229   high-resolution structural information for both montage and individual tile tomograms.

230   Ultimately, montage tomography solutions will help bridge the resolution gap and field of

231   view losses present between multi-modal microscopy imaging pipelines.

232

241

242   **Author contributions.** J.E.Y. and E.R.W. conceived and designed the study. M.R.L,

243   J.E.Y, E.R.W developed TomoGrapher and pre-processing workflow. J.E.Y., B.S.S,

244   J.Y.K., D.P., J.M.S., V.P., A.K., K.C., A.K., K.T. prepared the samples, performed the

245   experiments, and data processing. J.E.Y. and E.R.W. wrote the manuscript, with

246   contributions from all authors. All authors read and approved the manuscript.

247

248 **Competing Interests.** The funders had no role in study design, data collection and

249 interpretation, or the decision to submit the work for publication. The authors declare no

250 competing financial or non-financial interests.

References

1   Kühlbrandt, W. The Resolution Revolution. *Science* **343**, 1443-1444, doi:10.1126/science.1251652 (2014).

2   Turk, M. & Baumeister, W. The promise and the challenges of cryo-electron tomography. *FEBS Letters* **594**, 3243-3261, doi:https://doi.org/10.1002/1873-3468.13948 (2020).

3   Thompson, R. F., Walker, M., Siebert, C. A., Muench, S. P. & Ranson, N. A. An introduction to sample preparation and imaging by cryo-electron microscopy for structural biology. *Methods* **100**, 3-15, doi:10.1016/j.ymeth.2016.02.017 (2016).

4   Kiss, G. *et al.* Structural analysis of respiratory syncytial virus reveals the position of M2-1 between the matrix protein and the ribonucleoprotein complex. *J Virol* **88**, 7602-7617, doi:10.1128/jvi.00256-14 (2014).

5   Schur, F. K. M. Toward high-resolution in situ structural biology with cryo-electron tomography and subtomogram averaging. *Curr. Opin. Struct. Biol.* **58**, 1-9, doi:https://doi.org/10.1016/j.sbi.2019.03.018 (2019).

6   Al-Amoudi, A. *et al.* Cryo-electron microscopy of vitreous sections. *EMBO J* **23**, 3583-3588, doi:10.1038/sj.emboj.7600366 (2004).

7   Rigort, A. *et al.* Micromachining tools and correlative approaches for cellular cryo-electron tomography. *J. Struct. Biol.* **172**, 169-179, doi:https://doi.org/10.1016/j.jsb.2010.02.011 (2010).

8   Hampton, C. M. *et al.* Correlated fluorescence microscopy and cryo-electron tomography of virus-infected or transfected mammalian cells. *Nat. Protoc.* **12**, 150-167, doi:10.1038/nprot.2016.168 (2017).

9   Arnold, J. *et al.* Site-Specific Cryo-focused Ion Beam Sample Preparation Guided by 3D Correlative Microscopy. *Biophys. J.* **110**, 860-869, doi:https://doi.org/10.1016/j.bpj.2015.10.053 (2016).

10   Phan, S., Terada, M. & Lawrence, A. Serial reconstruction and montaging from large-field electron microscope tomograms. *Annu Int Conf IEEE Eng Med Biol Soc* **2009**, 5772-5776, doi:10.1109/IEMBS.2009.5332531 (2009).

11   Iancu, C. V. *et al.* A "flip–flop" rotation stage for routine dual-axis electron cryotomography. *J. Struct. Biol.* **151**, 288-297, doi:https://doi.org/10.1016/j.jsb.2005.07.004 (2005).

12   Shannon, C. E. Communication in the Presence of Noise. *Proceedings of the IRE* **37**, 10-21, doi:10.1109/JRPROC.1949.232969 (1949).

13   Faruqi, A. R. & McMullan, G. Direct imaging detectors for electron microscopy. *Nuclear Instruments and Methods in Physics Research Section A: Accelerators, Spectrometers, Detectors and Associated Equipment* **878**, 180-190, doi:https://doi.org/10.1016/j.nima.2017.07.037 (2018).

14   Baldwin, P. R. *et al.* Big data in cryoEM: automated collection, processing and accessibility of EM data. *Current Opinion in Microbiology* **43**, 1-8, doi:10.1016/j.mib.2017.10.005 (2018).

15   Peck, A. *et al.* Montage electron tomography of vitrified specimens. *bioRxiv*, 2021.2011.2002.466666, doi:10.1101/2021.11.02.466666 (2021).

294   16   Chen, R. *et al.* EPiK-a Workflow for Electron Tomography in Kepler. *Procedia Comput Sci*
295   **20**, 2295-2305, doi:10.1016/j.procs.2014.05.214 (2014).

296   17   Mastronarde, D. N., van der Heide, P. A., Morgan, G. P. & Marsh, B. J. Supermontaging:
297   Reconstructing Large Cellular Volumes by Stitching Together Laterally Adjacent
298   Tomograms. *Microsc Microanal.* **14**, 106-107, doi:10.1017/S1431927608086820 (2008).

299   18   Phan, S. *et al.* TxBR montage reconstruction for large field electron tomography. *J. Struct.*
300   *Biol.* **180**, 154-164, doi:https://doi.org/10.1016/j.jsb.2012.06.006 (2012).

301   19   Mastronarde, D. N. Automated electron microscope tomography using robust prediction
302   of specimen movements. *J. Struct. Biol.* **152**, 36-51, doi:10.1016/j.jsb.2005.07.007 (2005).

303   20   Fukushima, K., Kawakatsu, H. & Fukami, A. Fresnel fringes in electron microscope images.
304   *Journal of Physics D: Applied Physics* **7**, 257-266, doi:10.1088/0022-3727/7/2/310 (1974).

305   21   Cope, J., Heumann, J. & Hoenger, A. Cryo-electron tomography for structural
306   characterization of macromolecular complexes. *Curr Protoc Protein Sci* **Chapter 17**,
307   Unit17.13-Unit17.13, doi:10.1002/0471140864.ps1713s65 (2011).

308   22   Kremer, J. R., Mastronarde, D. N. & McIntosh, J. R. Computer Visualization of Three-
309   Dimensional Image Data Using IMOD. *J. Struct. Biol.* **116**, 71-76,
310   doi:https://doi.org/10.1006/jsbi.1996.0013 (1996).

311   23   Bouvette, J. *et al.* Beam image-shift accelerated data acquisition for near-atomic
312   resolution single-particle cryo-electron tomography. *Nat. Commun.* **12**, 1957,
313   doi:10.1038/s41467-021-22251-8 (2021).

314   24   Yang, J. E., Larson, M. R., Sibert, B. S., Shrum, S. & Wright, E. R. CorRelator: Interactive
315   software for real-time high precision cryo-correlative light and electron microscopy. *J*
316   *Struct Biol*, 107709, doi:10.1016/j.jsb.2021.107709 (2021).

317   25   Hu, M. *et al.* Respiratory syncytial virus co-opts host mitochondrial function to favour
318   infectious virus production. *eLife* **8**, e42448, doi:10.7554/eLife.42448 (2019).

319   26   Ke, Z. *et al.* The Morphology and Assembly of Respiratory Syncytial Virus Revealed by
320   Cryo-Electron Tomography. *Viruses* **10**, doi:10.3390/v10080446 (2018).

321   27   Bahadar, H., Maqbool, F., Niaz, K. & Abdollahi, M. Toxicity of Nanoparticles and an
322   Overview of Current Experimental Models. *Iran Biomed J* **20**, 1-11,
323   doi:10.7508/ibj.2016.01.001 (2016).

324   28   Klein, S. *et al.* Post-correlation on-lamella cryo-CLEM reveals the membrane architecture
325   of lamellar bodies. *Communications Biology* **4**, 137, doi:10.1038/s42003-020-01567-z
326   (2021).

327   29   Toro-Nahuelpan, M. *et al.* Tailoring cryo-electron microscopy grids by photo-
328   micropatterning for in-cell structural studies. *Nat. Methods* **17**, 50-54,
329   doi:10.1038/s41592-019-0630-5 (2020).

330   30   Sibert, B. S., Kim, J. Y., Yang, J. E. & Wright, E. R. Micropatterning Transmission Electron
331   Microscopy Grids to Direct Cell Positioning within Whole-Cell Cryo-Electron Tomography
332   Workflows. *JoVE*, e62992, doi:doi:10.3791/62992 (2021).

333   31   Wolf, S. G. *et al.* 3D visualization of mitochondrial solid-phase calcium stores in whole
334   cells. *eLife* **6**, e29929, doi:10.7554/eLife.29929 (2017).

335   32   Xiong, Q., Morphew, M. K., Schwartz, C. L., Hoenger, A. H. & Mastronarde, D. N. CTF
336   determination and correction for low dose tomographic tilt series. *J. Struct. Biol.* **168**, 378-
337   387, doi:10.1016/j.jsb.2009.08.016 (2009).

338 33   Stobart, C. C. *et al.* A live RSV vaccine with engineered thermostability is immunogenic in
339   cotton rats despite high attenuation. *Nat. Commun.* **7**, 13916, doi:10.1038/ncomms13916
340   (2016).
341

Methods section only

342
343
344 34   Egger, B., van Giesen, L., Moraru, M. & Sprecher, S. G. In vitro imaging of primary neural
345   cell culture from Drosophila. *Nat. Protoc.* **8**, 958-965, doi:10.1038/nprot.2013.052 (2013).
346 35   Lu, W., Lakonishok, M. & Gelfand, V. I. Kinesin-1-powered microtubule sliding initiates
347   axonal regeneration in Drosophila cultured neurons. *Mol. Biol. Cell* **26**, 1296-1307,
348   doi:10.1091/mbc.E14-10-1423 (2015).
349 36   Bieber, A., Capitanio, C., Wilfling, F., Plitzko, J. & Erdmann, P. S. Sample Preparation by
350   3D-Correlative Focused Ion Beam Milling for High-Resolution Cryo-Electron Tomography.
351   *JoVE*, e62886, doi:doi:10.3791/62886 (2021).
352 37   Wagner, F. R. *et al.* Preparing samples from whole cells using focused-ion-beam milling
353   for cryo-electron tomography. *Nat. Protoc.* **15**, 2041-2070, doi:10.1038/s41596-020-
354   0320-x (2020).
355 38   Gorelick, S. *et al.* PIE-scope, integrated cryo-correlative light and FIB/SEM microscopy.
356   *eLife* **8**, e45919, doi:10.7554/eLife.45919 (2019).
357 39   Reisinger, T., Leufke, P. M., Gleiter, H. & Hahn, H. On the relative intensity of Poisson's
358   spot. *New Journal of Physics* **19**, 033022, doi:10.1088/1367-2630/aa5e7f (2017).
359 40   Weis, F., Hagen, W. J. H., Schorb, M. & Mattei, S. Strategies for Optimization of Cryogenic
360   Electron Tomography Data Acquisition. *JoVE*, e62383, doi:doi:10.3791/62383 (2021).
361 41   Zheng, S. Q. *et al.* MotionCor2: anisotropic correction of beam-induced motion for
362   improved cryo-electron microscopy. *Nat. Methods* **14**, 331-332, doi:10.1038/nmeth.4193
363   (2017).
364 42   Mastronarde, D. N. & Held, S. R. Automated tilt series alignment and tomographic
365   reconstruction in IMOD. *J Struct Biol* **197**, 102-113, doi:10.1016/j.jsb.2016.07.011 (2017).
366 43   Grant, T. & Grigorieff, N. Measuring the optimal exposure for single particle cryo-EM using
367   a 2.6 Å reconstruction of rotavirus VP6. *eLife* **4**, e06980, doi:10.7554/eLife.06980 (2015).
368 44   Moreno, J. J., Martínez-Sánchez, A., Martínez, J. A., Garzón, E. M. & Fernández, J. J.
369   TomoEED: fast edge-enhancing denoising of tomographic volumes. *Bioinformatics* **34**,
370   3776-3778, doi:10.1093/bioinformatics/bty435 (2018).
371 45   Chen, M. *et al.* Convolutional neural networks for automated annotation of cellular cryo-
372   electron tomograms. *Nat. Methods* **14**, 983-985, doi:10.1038/nmeth.4405 (2017).
373 46   Rohou, A. & Grigorieff, N. CTFFIND4: Fast and accurate defocus estimation from electron
374   micrographs. *J. Struct. Biol.* **192**, 216-221, doi:https://doi.org/10.1016/j.jsb.2015.08.008
375   (2015).
376 47   Nicastro, D. *et al.* The molecular architecture of axonemes revealed by cryoelectron
377   tomography. *Science* **313**, 944-948, doi:10.1126/science.1128618 (2006).
378 48   Liljeroos, L., Krzyzaniak, M. A., Helenius, A. & Butcher, S. J. Architecture of respiratory
379   syncytial virus revealed by electron cryotomography. *Proc Natl Acad Sci USA* **110**, 11133,
380   doi:10.1073/pnas.1309070110 (2013).

381 49 McLellan Jason, S. *et al.* Structure of RSV Fusion Glycoprotein Trimer Bound to a
382   Prefusion-Specific Neutralizing Antibody. *Science* **340**, 1113-1117,
383   doi:10.1126/science.1234914 (2013).
384 50 Pettersen, E. F. *et al.* UCSF Chimera--a visualization system for exploratory research and
385   analysis. *J Comput Chem* **25**, 1605-1612, doi:10.1002/jcc.20084 (2004).
386

387

388 **Methods.**

389 **Cell lines and cell culture.** HeLa cells (ATCC CCL-2, ATCC, Manassas, VA, USA) and

390 A549 cells (ATCC, CCL-185) were cultured and maintained in supplemented DMEM

391 complete medium and BEAS-2B cells (ATCC, CRL-9609) cultured in supplemented

392 RPMI-1640 complete medium as reported previously[26]. Primary *Drosophila melanogaster*

393 third-instar larval neurons (the strain elaV-Gal4, UAS-CD8::GFP maintained and kindly

394 provided by the Wildonger lab, UCSD) were extracted, cultured in supplemented

395 Schneider's media, and maintained on micropatterned grids as previously described[34].

396

397 **Cell seeding, infection and *in-situ* labeling on TEM grids.** Cell seeding on the TEM

398 grids was performed following previous reports[26]. Briefly, Quantifoil grids (200 mesh Au

399 R2/2 carbon or SiO_2 film; Quantifoil Micro Tools GmbH, Großlöbichau, Germany) were

400 coated with extra carbon (5 to 8 nm) and glow discharged (10 mA, 60 sec). HeLa and

401 BEAS-2B cells were trypsinized and seeded at a density of 0.7 X 10^5 cells/mL, followed

402 by an overnight incubation prior to subsequent applications. For montage cryo-ET and

403 correlative cryo-FLM-montage-ET, HeLa and BEAS-2B cells on the grids were infected

404 with the recombinant virus strain RSV rA2-mK$^+$ at an optimized multiplicity of infection

405 (M.O.I.) of 10 for 24 hours at 37 °C and 5 % CO_2, as determined previously[26]. For cryo-

406 focused ion beam milling (FIB-milling), A549 cells were digested and seeded at a density

407 of 0.3 X 10^5 cells/mL on SiO_2 Au Quantifoil grids for 16 to 24 hours.

408

409 **Micropatterning and neuron cell culture on TEM grids.** Micropatterning and culturing

410 of primary *Drosophila* larval neurons was performed as described[30]. Briefly, the extra

411 carbon coated gold Quantifoil grids (200 mesh, R 1.2/20, holey carbon film; Quantifoil

412 Micro Tools GmbH, Großlöbichau, Germany) were glow-discharged, and coated with

413 0.05% poly-L-Lysine (PLL). The grids were then functionalized by applying a layer of anti-

414 fouling polyethylene glycol-succinimidyl valerate (PEG-SVA), followed by application of a

415 photocatalyst reagent, 4-benzoylbenzyl-trimethylammonium chloride (PLPP) gel.

416 Maskless photopatterning was performed to ablate the anti-fouling layer in defined

417 patterns with a UV laser (λ = 375 nm, at a dose of 30 mJ/mm^2) using an Alvéole PRIMO

418 micropatterning system. Adherent extracellular matrix (ECM) protein, fluorescently-

419 labeled concanavalin A, Alexa Fluor™ 350 conjugate (emission, λ = 457 nm, 0.5 mg/mL

420 in water or PBS, ThermoFisher Scientific), was then added to promote the cellular

421 adhesion and growth of primary *Drosophila* larval neurons isolated and cultured according

422 to established protocols[34,35]. These neurons had pan-neuronal GFP expression

423 (emission, λ = 525 nm) on the membrane (CD8-GFP) to allow for tracking using live-cell

424 wide-field fluorescent microscopy imaging. Neurons on patterned grids grew for a

425 minimum of 48-72 hours for neurite growth prior to plunge freezing.

426

427 **Vitrification.** For EM grids prepared for non-FIB cryo-ET applications, 4 μl of 10 nm BSA-

428 treated gold fiducial beads (Aurion Gold Nanoparticles, Electron Microscopy Sciences,

429 PA, USA) were applied before vitrification. The grids were plunge-frozen using either a

430 Gatan CryoPlunge3 system (CP3) with GentleBlot blotters (Gatan, Inc., Pleasanton, CA,

431 USA) or a Leica EM GP (Leica Microsystems). The Gatan CP3 system was operated at

432 75 ~ 80 % humidity and a blot time of 4.5 to 5.5 s for double-sided blotting and plunge

433 freezing. The Leica EM GP plunger was set to 25 °C to 37 °C, 99% humidity and blot

434   times of 6 s for R 1.2/20 micropatterned carbon-foil grids, and 15 s for R2/2 SiO_2 foil grids

435   for single-sided blotting and plunge freezing. Plunge-frozen grids were then clipped and

436   stored in cryo-grid boxes under liquid nitrogen.

437

438   **Correlative live-cell and cryogenic fluorescent microscopy.** Healthy A549 or RSV-

439   infected HeLa cells were stained with MitoTrackerGreen FM (M7514, ThermoFisher

440   Scientific, 100 nM, 30 min at 37 °C and 5 % CO_2), washed, and stained with Hoechst-

441   33342 (H3570, ThermoFisher Scientific, 1 to 1000 dilution, 20 min at 37 °C and 5 % CO_2)

442   to visualize mitochondria and the nucleus. As reported previously[8], live-cell wide-field

443   imaging (20 X, 0.4NA lens, dry) and cryo-FLM (50 X, ceramic-tipped, 0.9NA lens) on

444   vitrified samples were performed on a Leica DMi8 and Leica EM Cryo-CLEM THUNDER

445   system, respectively. The brightfield and band pass filter cubes of GFP (emission, λ =

446   525 nm), DAPI (emission, λ = 477 nm), Texas Red (emission, λ = 619 nm), and Y5

447   (emission, λ = 660 nm) were used. Live-cell wide-field images were collected as a grid

448   montage at 20X. For cryo-FLM, Z-stack projections of 12 to 15 μm for each channel were

449   collected on the vitrified sample at a Nyquist sampling step of 350 nm using the Leica

450   LAS X software. Small Volume Computational Clearance (SVCC) from the Leica LAS X

451   THUNDER package was applied for fluorescent image deconvolution and blurring

452   reduction on the cryo-FLM image stacks. All images and mosaics were exported and used

453   as LZW compressed lossless 16-bit TIFF format. The on-the-fly cryo-FLM to cryo-ET

454   correlation and data collection was performed using CorRelator[24]. Grids that were imaged

455   under cryogenic conditions were saved and stored in in cryo-grid boxes under liquid

456   nitrogen.

457

458   **3D targeted Cryo-FIB-SEM.** Low toxic nanoparticles of 40 nm (FluoSpheres, carboxylate

459   modified microsphere, dark red fluorescent (660/680 nm), ThermoFisher Scientific,

460   F8789) were introduced to cells seeded on the grid for an incubation of 2 hours at 2

461   mg/mL, followed by washing with 1X PBS and 5 min incubation of 5 ~10 % glycerol as a

462   cryoprotectant to properly vitrify cells. Afterwards, 4 μl of diluted 200 nm FluoSpheres (1

463   to 200 dilution, dark red fluorescent (660/670 nm), ThermoFisher Scientific, F8807) were

464   applied to the grid in the humidity chamber of the Leica EM GP plunger prior to the

465   vitrification step. Following Leica EM Cryo CLEM THUNDER imaging, clipped grids were

466   transferred into a dual-beam (SEM/FIB) Aquilos2 cryo-FIB microscope (ThermoFisher

467   Scientific) operating under cryogenic conditions. To improve the sample conductivity and

468   reduce the curtaining artifacts during FIB milling, the grid was first sputter-coated with

469   platinum (10 mA, 15 to 30 sec), and then coated with organometallic platinum using the

470   in-chamber gas injection system (GIS, 6 sec with a measured deposition rate of 600

471   nm/sec). A 2D affine transformation on the XY plane was performed to align cryo-FLM

472   and cryo-scanning electron microscopy (SEM) grid mosaics on a rough micron scale and

473   to further correlate square images from two modalities on a fine nanometer scale

474   precision using hole centroids or 200 nm FluoSpheres in CorRelator. The eucentric height

475   of the region of interest on the cryo-shuttle inside the dual-beam microscope and a

476   shallow FIB-milling angle of 8 to 12° were determined. 2D SEM and FIB views of the

477   squares (with the field of view large enough to include sufficient external microspheres

478   and features as registration points) that contained the region of interest (ROI) were

479   collected at the eucentric height and milling angle. 3D coordinate transform between the

480   3D Z-stack of the Y5 channel (nanoparticles, emission λ = 680 nm) and the 2D FIB view

481   was conducted through the optimized rigid body 3D transformation algorithm available in

482   the 3DCT package using external 200 nm FluoSpheres (n = 4 to 10) as registration

483   points[36]. The transformed coordinates (X, Y, Z) were then imported into CorRelator to fine

484   tune the deviations in X and Y coordinates introduced by the Z transformation in 3DCT,

485   using the closed-form best-fitting least-square solution. The FIB milling boxes were

486   positioned based on the prediction in the 2D FIB view in CorRelator[24]. The ion-beam

487   milling process was performed using 0.3 nA for rough milling and gradually decreased

488   currents of 0.1 nA, 50 pA, 30 pA, and 10 pA, following previously established protocols[37].

489   Without changing the sample/shuttle position during the milling, a series of cryo-SEM

490   images (electron beam set at 2 kV, 25 pA, dwell time of 1 μs) were collected as the lamella

491   was thinned from an initial thickness of 5 μm, 3 μm, 1 μm, to 800 nm, 500 nm and to the

492   final 200 nm. The SEM images were used to: 1) check the milling process related to stage

493   drift, lamella bending, etc., 2) adjust the milling positions by visualizing the density of

494   internalized 40 nm nanoparticles on the lamella and comparing their positions (X, Y in

495   ~100 to 200 nm deviation error, and 500 nm in Z relative to the ROI) in the correlated

496   FLM Z-stack, and 3) to confirm the successfully milled isolated region houses the ROI.

497   On-the-fly monitoring of nanoparticle presence provided quick and movement-free

498   feedback on 3D targeted milling when an integrated FLM system is not available. It could

499   also help eliminate excessive alignment steps introduced by shuttle moving in an

500   integrated FLM and FIB-SEM system when the sample is moved back and forth between

501   the FLM imaging and FIB-SEM positions[38].

502

503   To further confirm the preservation of an ROI in the lamella, lamella were transferred to

504   the Leica EM Cryo-CLEM THUNDER system and a Z-stack of the same channels was

505   collected. Post-correlations on lamella of cryo-FLM, cryo-SEM, and cryo-EM were

506   performed using angle-corrected neighboring signals around the lamella to transform

507   cryo-FLM signals to corresponding features on the lamella under cryo-SEM and cryo-EM

508   as described previously[28].

509

510   **Cryo-electron tomography and reconstructions.** After live-cell FLM, cryo-FLM

511   imaging, and/or cryo-FIB milling, the same clipped frozen grids were imaged using a Titan

512   Krios (ThermoFisher Scientific, Hillsboro, OR, USA) at 300 kV. Images were acquired on

513   a Gatan Bioquantum GIF-K3 camera in EFTEM mode using a 20 eV slit. Images were

514   captured at various magnifications of 81x (4485 Å/pixel) for whole grid mosaic collection,

515   470x (399 Å/pixel) and 1950x (177.6 Å/pixel) for square or whole lamella overview, 6500x

516   (27.4 Å/pixel) for intermediate magnification imaging where the field of view is suitable for

517   reliable tracking and 40 nm nanoparticles are visibly distinguished, and 19500x (4.603

518   Å/pixel) for data acquisition using the SerialEM software package[19]. The full frame size of

519   5760 x 4092 pixels (counting, CDS mode at 10 eps of dose rate) was collected.

520

521   *Montage cryo-ET setup in SerialEM.* Regular image-shift montage acquisition and the

522   multiple record function in SerialEM were adapted for implementation of overlapped

523   beam-image shift tiling. Benchmarks were done at a data acquisition magnification (pixel

524   size of 4.603 Å/pixel) typical for cryo-ET. The illuminated area of 3.1 μm in diameter on

525   the sample was determined by the beam size on the camera and the lens magnification.

526   Fresh gains were collected with this beam size (3.1 μm) and the gain normalized image

527   over vacuum was low pass filtered to 50 Å to enhance the signal of Fresnel fringe peaks.

528   Based on the behaviors of Fresnel fringes[39] and EM Gaussian signal distribution, the

529   intensity value of the image over pixel was fitted into two distribution curves, a Poisson

530   curve (maximum likelihood estimate/peak λ) to fit the edge areas considered as "signal

531   peaks" using 20% of X and Y dimension extending from the edge towards the center, and

532   a Gaussian curve ($\mu \pm 2\sigma$) to fit the center area considered as noise/background using

533   90% of whole X and Y dimension from the center towards the edge with a 10% overlap

534   with the "edge" area in MatLab (*poissfit* and *gaussianFit* Curve Fitting Toolbox,

535   MathWorks, Natick, MA, USA). The cut-off from "signal" to "noise" were determined as

536   the possibility of "signal" peaks fading into $\mu \pm 2\sigma$ of "noise" distribution. From multiple

537   measurements (n $\geq$ 3) along the circular beam edge, the cut-off was 3.5 ~4 % of X

538   extending from the edge and insignificant in the Y direction. Thus, the rest of the image

539   was considered as a fringeless FOV. Over a wide range of samples, we selected the pixel

540   overlaps of 15% to 20% in the fringe-affected X-direction and 10% in the fringe-free Y-

541   direction as the optimal tiling strategy, such that the usable field of view per camera frame

542   was maximized after correction of Fresnel fringes and optimization of the pre-exposed

543   area outside of camera frame FOV. A regular montage with minimum dimensions of 2X2

544   was collected with the designated overlaps in X and Y at the data acquisition

545   magnification. A rigorous and reliable image shift calibration in SerialEM at the data

546   acquisition magnification was performed and repeated to ensure a more accurate shift.

547   The beam-image shift tiling information (ImageShift entry under each item section in the

548   image metadata file ".mdoc" file) was obtained on-the-fly. The shift in the X direction to

549 achieve the frame overlap of 15 % in X was retrieved by calculating the difference in

550 image shift between the tile 1 (PieceCoordinates of 0 0 0) and tile 3 (PieceCoordinates of

551 4608 0 0). The shift in the y direction to achieve the frame overlap of 10 % overlap in Y

552 was retrieved by calculating the difference between tile 1 (PieceCoordinates of 0 0 0) and

553 tile 2 (PieceCoordinates of 0 3516 0). The MultishotParams (X/Y component of image

554 shift vector) was subsequently modified to reflect the tile montage image shift and saved

555 under the SerialEM setting file.

556

557 *Montage cryo-tilt series collection in SerialEM*. A SerialEM macro (available at

558 https://github.com/wright-cemrc-projects/cryoet-montage) was used to implement the

559 montage tilt series by acquiring overlapping tiles with designated overlaps to form a

560 montage at each tilt with an additional translational shift and or rotation shift to distribute

561 the dose. Autofocusing was performed at each tilt and shifted along the orientation of the

562 tilt axis 500 nm plus the maximum translational shift of the center of montage tile pattern

563 (e.g. 0.8 μm, Supplementary Figs. 9a) away from the edge of the montage tile pattern.

564 The total dose per tile tilt series was 30-40% below the maximum dose the sample was

565 able to tolerate before evidence of punctate bubbles. At the beginning of each grouped

566 tilt, high magnification/data acquisition tracking with a threshold of 5% of the FOV to

567 acquire a new tracking reference and to iterate the alignment until the threshold was met

568 (usually within one or two iterations), using the nearby autofocusing area, was performed.

569 An additional lower intermediate magnification tracking on a larger FOV of the region of

570 interest was implemented when the tilt angles were above 30°, with a threshold of a

571 difference greater than 10% (usually within one or two iterations). The tilt series collection

572   was paused when the iterations for convergence exceeded 5 times. Benchmarks were

573   done using a 3X3 or 3X4 montage tile pattern and a dose-symmetric scheme running at

574   $\pm$ 51° with 3° increments, groups of 3 tilts (original "Hagen scheme" is group of 1 tilt) and

575   a dose of 2 e$^-$/Å^2/tile per tilt for RSV-infected BEAS-2B and HeLa cells, and neurons on

576   micropatterned grids, while a dose of 1.42 e$^-$/Å^2/tile per tilt for A549 cell lamella based on

577   the dose tolerance measurements of each sample. The CDS counting mode and dose

578   rate of 10 eps were used on a K3 camera. The translational shift off-sets followed the

579   global spiral displacement (A_{final} = 1.5, Period = 3, Turns = 50, Revolutions = 15 as input

580   parameters to control the spiral size and resulting displacement offsets). The speed of

581   collection varied with the size of the montage tile, the type of microscope, detector used

582   and sample-dependent total dose. Benchmark collections were 60 min on average and

583   rendered 9 sub-tilt series (3X3 tile pattern) that were stitched seamlessly to form one

584   montaged tilt series. Translational spiral off-sets and collection schemes (bidirectional,

585   dose-symmetric, defocus, etc.) can be adjusted accordingly in the SerialEM macro. The

586   SerialEM macro can be modified to adjust translational spiral off-sets and collection

587   schemes (bidirectional, dose-symmetric, defocus, etc.). The macro can be integrated into

588   existing common automated data collection schemes using the function *Navigator*

589   *Acquire at points* in SerialEM[40].

590

591   *Montage tilt series processing*. All movie frames per acquisition (0.1~0.2 e$^-$/Å^2/frame)

592   were aligned and corrected using MotionCor2[41]. For montage tilt series, the total tiles per

593   tilt were registered and stitched together using the designated beam coordinates supplied

594   to the microscope as described above and with linear cross-correlation methods[42].

595   Despite the fringes on the edge, intrinsic low contrast and low dose received by cryo-tilt

596   series, the regularity of the montage tiling pattern and sufficient overlaps with optimized

597   tiling strategy consistently provided robust and automated seamless stitching without user

598   intervention up to $\pm$ 39°. Manual image alignment (MIDAS), implemented in the IMOD

599   package[42], was used to adjust piece coordinates and iteratively cross-correlate adjacent

600   tiles at higher tilts when necessary. Fully stitched montage tilt series were binned by 2.

601   Tilt series alignment and tomographic reconstructions were performed using the IMOD

602   package with a final pixel size of 9.206 Å. In the absence of gold fiducials in the FIB-milled

603   lamella, alignment of the tilt series was performed using patch tracking or internalized

604   nanoparticles as tracking markers. CTF correction using ctfplotter and ctfphaseflip and

605   dose-weighted filtering[43] were applied to the aligned tilt series prior to tomogram

606   reconstruction. For segmentation, the aligned tilt series were further binned 3X (final pixel

607   size of 27.6 Å, binned 6X) prior to the tomogram reconstruction. Tomograms were either

608   processed using fast edge-enhancing denoising algorithm based on anisotropic nonlinear

609   diffusion implemented in TomoEED[44] or Gaussian low-pass filtered to 80 Å for

610   visualization and segmentation. Tomograms of stitched montage tilt series (final pixel size

611   of 27.6 Å) were annotated using convolutional neural networks implemented in the

612   EMAN2 package[45]. For the sub-tilt series, motion-corrected frames were sorted to

613   generate individual tile tilt series that were CTF estimated using CTFFIND4[46]. Tilt series

614   that contained one or more inadequate projections (not properly tracked or failed CTF

615   estimation) were discarded. Qualified sub-tilt series were then aligned, CTF corrected

616   with ctfplotter and ctfphaseflip, dose-weighted filtered, binned to 2X (a final pixel size of

617   9.206 Å), and reconstructed into tomograms, similar to stitched montage tilt series

618   implemented in the IMOD package. Python or bash scripts (available at

619   https://github.com/wright-cemrc-projects/cryoet-montage) were used to automate the

620   movie frame alignment, montage tile stitching, sub-tilt and montage tilt generation.

621

622   **Sub-tomogram averaging.** For proof of concept, all averaging was done on unfiltered

623   sub-tilt tomograms using PEET 1.15.0[47], following the steps reported previously[33].

624   Particles were manually picked from low pass filtered sub-tilt tomograms binned 2X to a

625   final pixel size of 9.206 Å. Initial particle orientation and rotation axes of particles were

626   generated using SpikeInit (PEET). An initial alignment was done with 565 particles from

627   one tomogram using post-fusion F glycoprotein (EMDB-2393)[48] low pass filtered to 60 Å

628   as the initial reference. The final average from this first run was low pass filtered to 60 Å

629   and used as the initial reference for a second run on 12,435 particles from a total of 12

630   sub-tilt tomograms, with a soft-edged cylinder mask applied during the alignment.

631   Duplicate particles were removed during each iteration with a tolerance of 73.6 Å (8

632   voxels). An additional iteration was done with refined particles using a smaller search

633   range and a larger mask with softer edges. The final average from the second run

634   suggested a three-fold symmetry, consistent with reported crystal structures[49]. C3

635   symmetry was imposed using *modifyMotiveList* in PEET to generate a three-fold

636   symmetric data set. The C3 symmetric data set was aligned and averaged using the final

637   average from the second run, low-pass filtered to 60 Å as the initial reference for

638   refinement with a smaller search range. The final sub-tomogram average (final pixel size

639   of 9.26 Å, binned 2X) from the C3 symmetry expanded particles was reconstructed from

640   23,259 particles. The final density map of F was low pass filtered to 29.53 Å based on the

641   FSC cutoff of 0.5 that was calculated in PEET. The picked particles that were in the

642   stitched area (15% in X and 10% in Y) were removed and the rest were reprocessed

643   following the same steps. The final sub-tomogram average (final pixel size of 9.26 Å,

644   binned 2X) from the C3 symmetry expanded particles was reconstructed from 20,707

645   particles. The final density map of F was low pass filtered to 27 Å based on the FSC cutoff

646   of 0.5 calculated in PEET. The atomic crystal model of pre-fusion F trimer (PDB: 4JHW)[49]

647   was fitted in the filtered electron density map in Chimera[50].

648

649   **TomoGrapher development.**

650   Simulations of the tiled montage imaging and electron beam exposures on a sample were

651   developed as a collection of C# classes built on the Unity 3D engine (version

652   2020.3.20f1). The simulation represents an array of M x N x O volumes called voxels as

653   a sample interacted by an electron beam. The canvas "stage" comprises of 150 x 150

654   voxels (X = Y = 150, Z = 1, total extent of 10 x 10 x 0.2 μm) with the center butterfly ROI

655   spanning across 5 x 4 μm on the imaging XY plane. An interactive GUI describes

656   parameters of the imaging including sampling pixel spacing, illuminated area of the beam

657   on the camera, the tiling pattern of the beam, tilt ranges, and translations defined by spiral

658   offsets. A complete run of a simulation iterates through each tilt increment across the

659   range, and ray traces from a sampling position of the illuminated area in the direction of

660   the beam to find intersections on the stage of voxel volumes. Voxels intersected by the

661   rays are aggregated in a set, and each voxel in the set has its total dose incremented

662   once per beam. The viewer provides a real-time animation of the beam shifts, tilting of

663   the stage, and overall exposure at each voxel. TomoGrapher release versions and source

664   code are available at https://github.com/wright-cemrc-projects/cryoet-montage .

665

666   **Statistics and Reproducibility.** Experiments performed in Figs. 1b-e, 2a-b,

667   Supplementary Figs. 2, 3b-c, 6, 8, 9 were performed independently three times with

668   similar results. Experiments from Figs. 1f, 2c-f, were performed in duplicates, resulting in

669   7 montaged tilt series on FIB lamellas from two lamellas on two different grids and 13

670   montaged tilt series on two different micropatterned neuron grids.
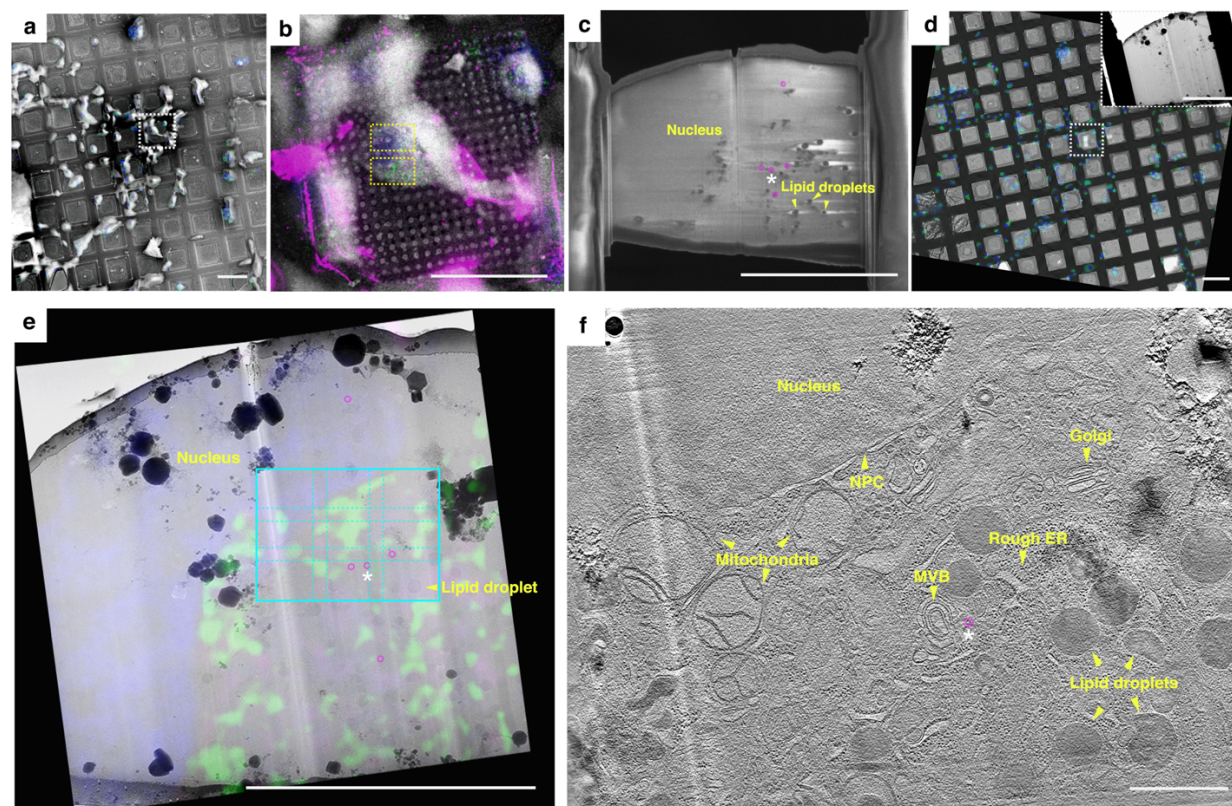
Figures and Legends

Fig. 1. Correlative cryo-FLM, cryo-FIB-SEM, and montage cryo-ET of a cryo-lamella from an A549 cell to visualize the in-situ architecture of the nucleus, mitochondria, and other organelles. a. Correlation of cryo-SEM and cryo-FLM grid mosaics to identify an A549 cell in the square of interest (white box). Scale bar, 100 μm. **b.** Cryo-FIB-milling boxes (pair of dashed yellow boxes) positioned to target the nucleus (blue) and mitochondria (green) in an A549 cell (white box in **a**), with internalized fluorescent beads (40 nm, pink) as milling "fiducials" for on-the-fly 3D targeted correlation. **c.** Cryo-SEM of the 200 nm thick lamella. Nucleus, lipid droplets, and internalized fluorescent beads (pink circles) are noted. Scale bars, 10 μm in **b** and **c. d.** Correlation of pre-FIB-milled cryo-FLM and post-FIB-milled cryo-TEM grid mosaics (Inset, cryo-TEM image of the lamella at higher magnification). Scale bars, 100 μm in **d**, 10 μm in inset of **d. e.** Post correlation overlay of the 2D cryo-EM image of the lamella with the corresponding Z section from the pre-FIB-milled cryo-FLM stack. A 3x3 tiling for montage cryo-ET (cyan, 6.8 x 5.3 μm at a pixel size of 4.603 Å) at the ROI. Scale bar, 10 μm. The same internalized fluorescent beads as in **c** (pink circles) are noted. **f.** Tomographic slice, ~45 nm thick (binned 2x tomogram at a pixel size of 9.206 Å), through the 3X3 montaged cellular tomogram (cyan ROI in **e**). Nucleus, nuclear pore complex (NPC), mitochondria, Golgi apparatus, rough ER, multivesicular bodies (MVB) are noted. Scale bar 1 μm. The same internalized fluorescent bead (pink circled) as in **c**, **e**, **f** was noted by the asterisk (white).
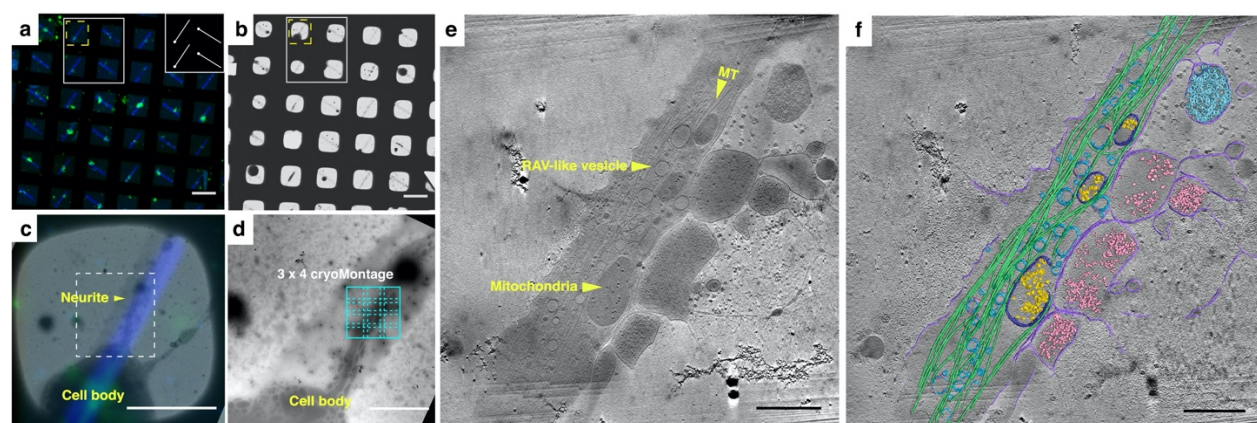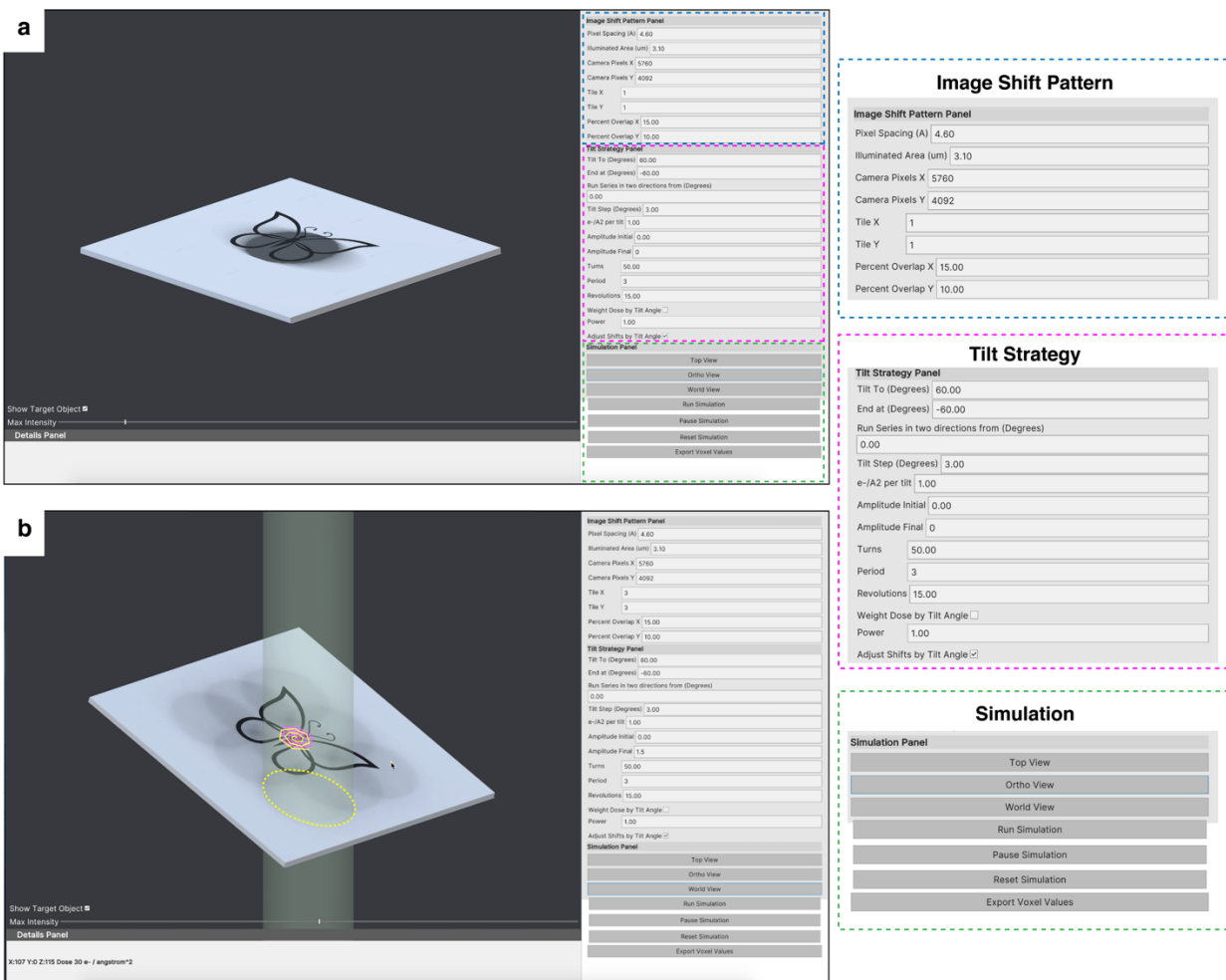
Fig. 2. Correlative live-cell-FLM and montage cryo-ET of primary *Drosophila melanogaster* neurons on a mask-free micropatterned cryo-TEM grid. a-b. Live-cell FLM (**a**) and cryo-EM (**b**) grid maps of membrane GFP-labeled primary neurons (green) cultured on a gold-mesh, holey (R1.2/20) carbon film micropatterned with a straight-line pattern (inset in **a**) across the grid and coated with fluorescent concanavalin A (blue) to control the growth of neurites. Scale bars, 100 μm. **c.** Overlay of correlated FLM-cryo-EM image of the square highlighted in yellow in **a** and **b**. **d.** Enlarged cryo-EM image of the dashed white boxed region in **c**. A 3X3 tiling for montage cryo-ET (cyan, 6.8 x 5.3 μm at a pixel size of 4.603 Å) on the region of interest (ROI) extending from the cell body. Scale bars, 50 μm in **c**, 10 μm in **d**. **e-f.** Tomographic slice of ~45 nm thick (binned 2x tomogram at pixel size of 9.206 Å), reconstructed from the 3X3 montage tilt series at the ROI (**e**) and the corresponding segmentation (**f**). The structured organization of microtubules (MT, green) and the arrangement of surrounding cellular organelles, including mitochondria (dark blue with calcium granules (yellow)), ribosomes (light pink) and ribosome-associated-like vesicles (darker cyan) are noted. Scale bars, 1 μm.

Supplementary Figures and Legends

3X3 stitched montage tilt series   Stitched 3x3 montage tomogram (enlarged view)
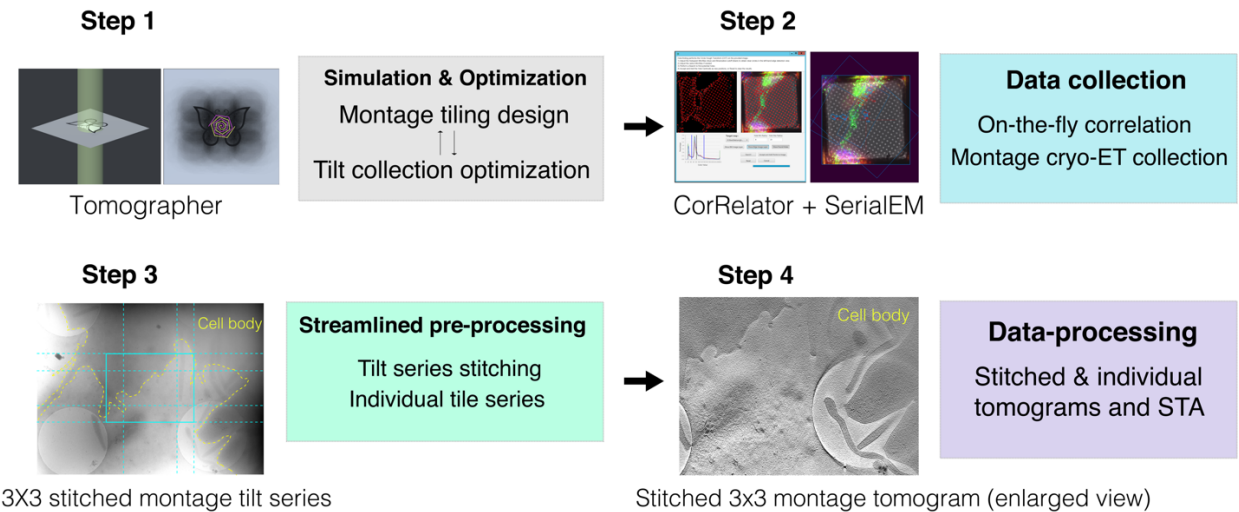
Supplementary Figure 1. Correlative montage cryo-electron tomography workflow. The correlative montage cryo-electron tomography (cryo-ET) workflow follows four main steps: **Step 1.** *TomoGrapher* simulation-guided tiling design and optimization of tiling patterns for cryo-ET data collection. **Step 2.** CorRelator-driven 2D and 3D cryo-correlation for high-accuracy targeting to support cryogenic tilt series collection with SerialEM. **Step 3.** Automated pre-processing to sort individual tiles and sub-tilt series, and stitch full montages concurrently with data collection. **Step 4.** Analyses including sub-tomogram averaging (STA) and segmentation may be conducted on both individual and stitched montage tomograms.

741
742

Supplementary Figure 2. Optimization of beam size and tiling strategy on a triple-condenser lens transmission electron microscope. Benchmarking of the montage cryo-ET workflow was done on a standard Titan Krios 300 kV microscope system with a K3 camera (5760 X 4092 pixels) at a pixel size of 4.603 Å, C2 aperture of 100 mm, and defocus of -5 μm. **a.** Fresnel fringes extending over the illuminated area (beam size 3.11 μm). ***Inset:*** Enlargement of the boxed fringe-containing area, low pass filtered to 50 Å. **b.** Radial intensity profile along the black line in the ***Inset*** of **(a)**. The region visibly impacted by the Fresnel fringes was determined to extend from the beam edge to ~200 pixels (grey area) towards the center of the image, affecting between 3.5 to 4 % of the outer edge of a tile. Based on the Fresnel fringes' Poisson behavior and TEM signal's gaussian distribution, the fringe peak intensities were fit to a Poisson curve (maximum likelihood estimate/peak λ), considered as "signal" and the fringeless illuminated area was fit to a gaussian function ($\mu \pm 2\sigma$) as "noise" in MatLab (*poissfit* and *gaussianFit* Curve Fitting Toolbox). The cut-off from "signal" to "noise" were determined as the possibility of "signal" peaks fading into $\mu \pm 2\sigma$ of "noise" distribution, from multiple measurements (n ≥ 3) along the circular beam edge. **c-e.** Optimization of beam size (1 to 5, beam sizes increase) in consideration of the full illuminated area (FIA), fringeless illuminated area, pre-exposed area, and captured field of view (FOV) at the constant benchmark magnification and defocus. **c.** The camera FOV (rectangle) and projected beam size (circles) extending outside viewable area. **d.** Linear relationships between illuminated areas on a triple-condenser lens Titan Krios system, defined as the electron beam projected onto the sample, and the beam projected size on the camera plane (orange line, orange circles in **c**, *r2* = 0.9989), and the associated fringeless illuminated area (black line, *r2* = 0.9995). **e.** The ratio of fringeless FOV captured on the camera over the full illuminated area (FIA). Overall, beam size 4 (3.11 μm) achieved reasonable fringeless illumination without wasting electron dose on unimaged yet illuminated sample area, and used for benchmark montage cryo-ET in the paper.

767

768

769
770
771 **Supplementary Figure 3. Simulation of tilt series collection in TomoGrapher GUI.**
772 *TomoGrapher* is a simulation tool providing a full 3D visualization of **(a)** single-shot and **(b)**
773 montaged (e.g., 3X3 tile) tilt series collection. A stage comprised of 150 x 150 x 1 voxels with a
774 target region of interest (ROI, butterfly, butterfly, 5 μm x 4 μm x 0.2 μm) shows the beam position
775 and accumulated dose values at each position of the total exposed area. The "Image Shift Pattern
776 Panel" (blue boxed) provides parameters to adjust the pixel size, illuminated area (beam size),
777 camera dimensions, and number of and percent overlap for the montage tiles. The "Tilt Strategy
778 Panel" (magenta boxed) controls the tilt range, directionality, tilt step increment, dose per tilt, the
779 amplitudes and geometries of the spiral translational shifts during a tilt series, and provides
780 updated preview images of simulation parameters. Varying intensity as 1/cosine of tilt angle to a
781 certain power is a selectable option to *Weight Dose by Tilt Angle*. Scaling the X-axis shift offset
782 by the cosine of the tilt angle can also be enabled with *Adjust Shifts by Tilt Angle* where the Y-
783 axis is aligned as the tilt axis. The "Simulation Panel" (green boxed) has buttons to change the
784 viewing angle, start a simulation, and export data.
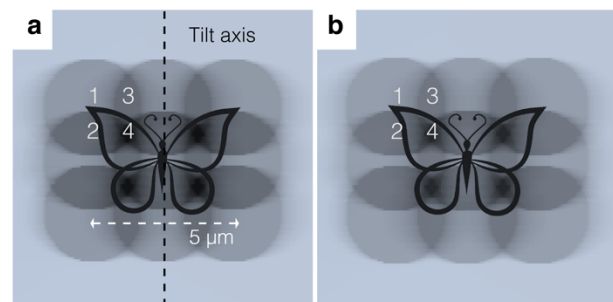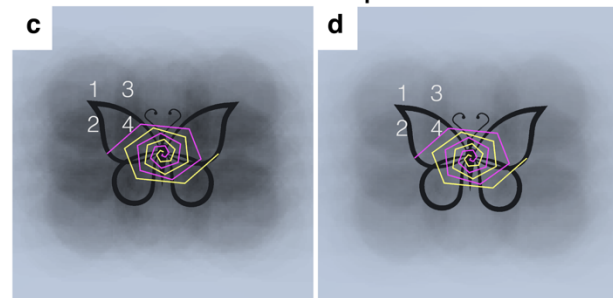
785
786
787

788
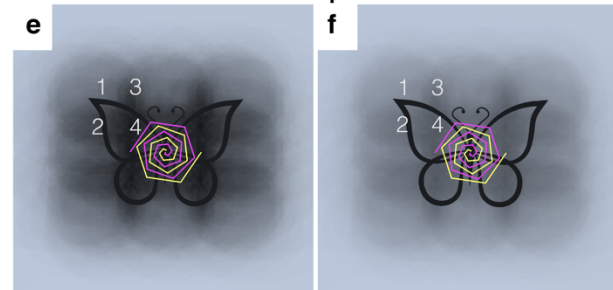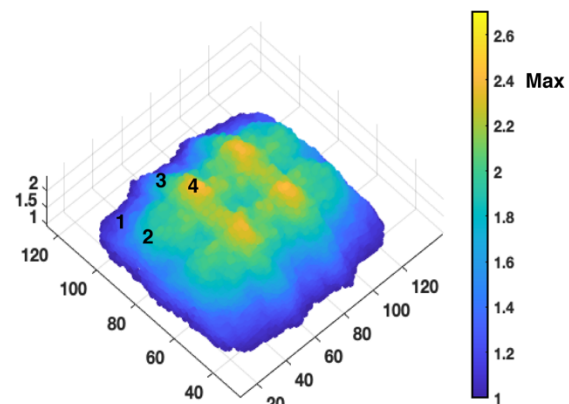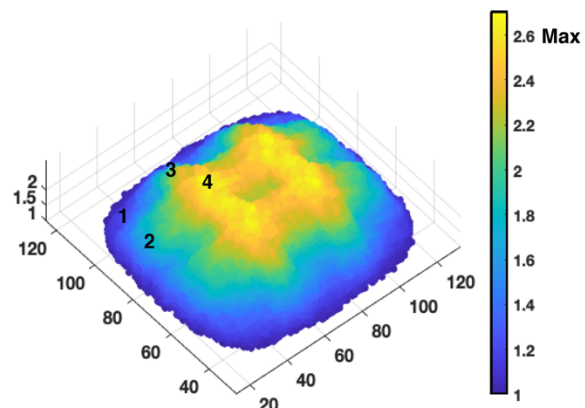
Supplementary Figure 4. Optimization of montage tiling translational shift for dose distribution in TomoGrapher. Simulated spatial distribution of dose accumulation in six montage tilt series collection schemes (3X3 tile pattern, pixel size of 4.603 Å, beam size of 3.1 μm, from -51° to 51° tilts with a 3° increment, the butterfly as ROI), with no translational offsets **(a, b)**, spiral translational offsets **(c, d)**, and the spiral translational shift with an optional scaling factor (cosine of tilt angle) to reduce x-axis shifts at higher tilt angles **(e, f)**. Values provided for dose are 1 e⁻/Å² per tile per tilt in **(a, c, d)** and 0.7 e⁻/Å² per tile per tilt in **(b, d, f)**. The accumulated dose at four areas (10 voxels pivoting around the central 1 to 4 points) were compared between the six collection schemes, detailed in **Supplementary Table 1**. The spiral shift pattern is delineated in pink (0° to 51°) and yellow (-51° to 0°) in **(c-f)** where the same global translational offset is applied (A_{final} = 2.5, Period = 3, Turns = 50, Revolutions = 15). **g-h.** Visualization of the dose distribution received by voxels of the ROI butterfly during the tilt series schemes applied in the benchmarking experiments (A_{final} = 1.5, Period = 3, Turns = 50, Revolutions = 15). The simulated dose values (e/Å²/voxel) were exported and plotted in MatLab to show the normalized distribution against the average dose of corresponding tiles from the no translational shift scheme. The same 1-4 center points are marked. The maximum (Max) normalized change is ~2.4-fold in **(g)** and ~2.6-fold in **(h)** with the axial scaling compensation. Height and color of each voxel correspond to its accumulated dose. No axial scaling compensation introduces larger shifts and more dose distribution due to the elliptical projection, but the scaling compensation distributes the dose more evenly.
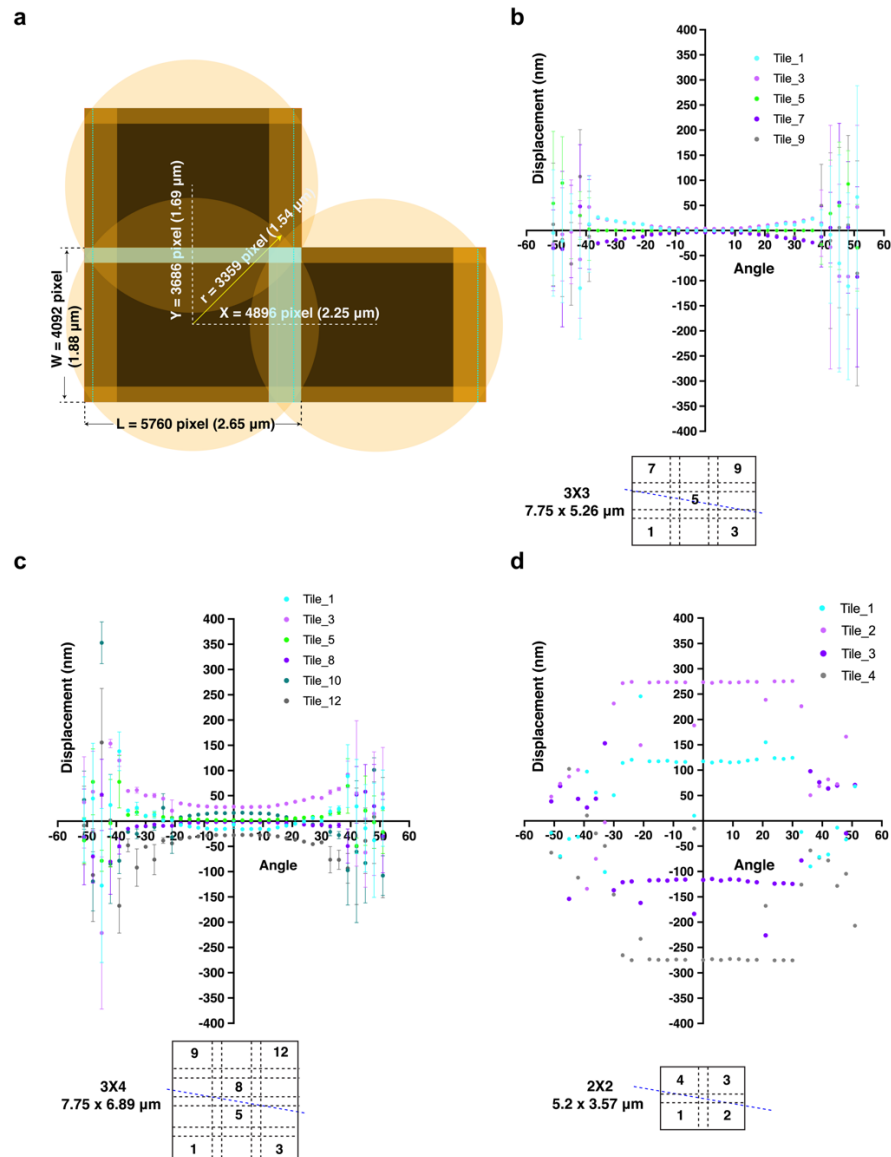
Supplementary Figure 5. Optimization of the tiling montage cryo-ET tilt series collection with global shift offsets to distribute the electron dose. a. Strategy for placement of beam tiles (fringeless usable camera FOV / FIA = 0.7) with 15% to 20% in X (Fresnel fringe-affected) and 10% in Y in a square or rectangular array after balancing fringes, pre-exposed area and the ratio of fringeless captured FOV over FIA. Higher overlap in X supports gap-free stitching under low-dose conditions. **b-d.** Shift displacement of individual tiles (blue dotted line notes the tilt axis) of tilt series collected using the benchmark imaging condition on a Titan Krios 300kV (pixel size of 4.603 Å, C2 aperture of 100 mm, defocus of -5 μm, tilt range of -51° to 51°, 3° increment, dose symmetric scheme with group of 3 tilt angles per switch) with application of an additional translation-only (3X3 in **b** and 3X4 in **c**, maximum global translational offsets of 0.8 μm, n = 8) or translation plus an additional 20° per tilt rotation offset (total rotation of 35 tilts x 20° = 700°) in (**d**, n = 1) for dose distribution. **d.** Representative plot of tile displacement for a montage tilt series including both translational and rotational shifts which introduce much larger displacements that reduce the effectiveness of automated montage stitching routines. The benchmark spiral

826   parameters (A_{final} = 1.5, Period = 3, Turns = 50, Revolutions = 15) resulted in a ~0.8 μm maximum
827   translational offset.

828
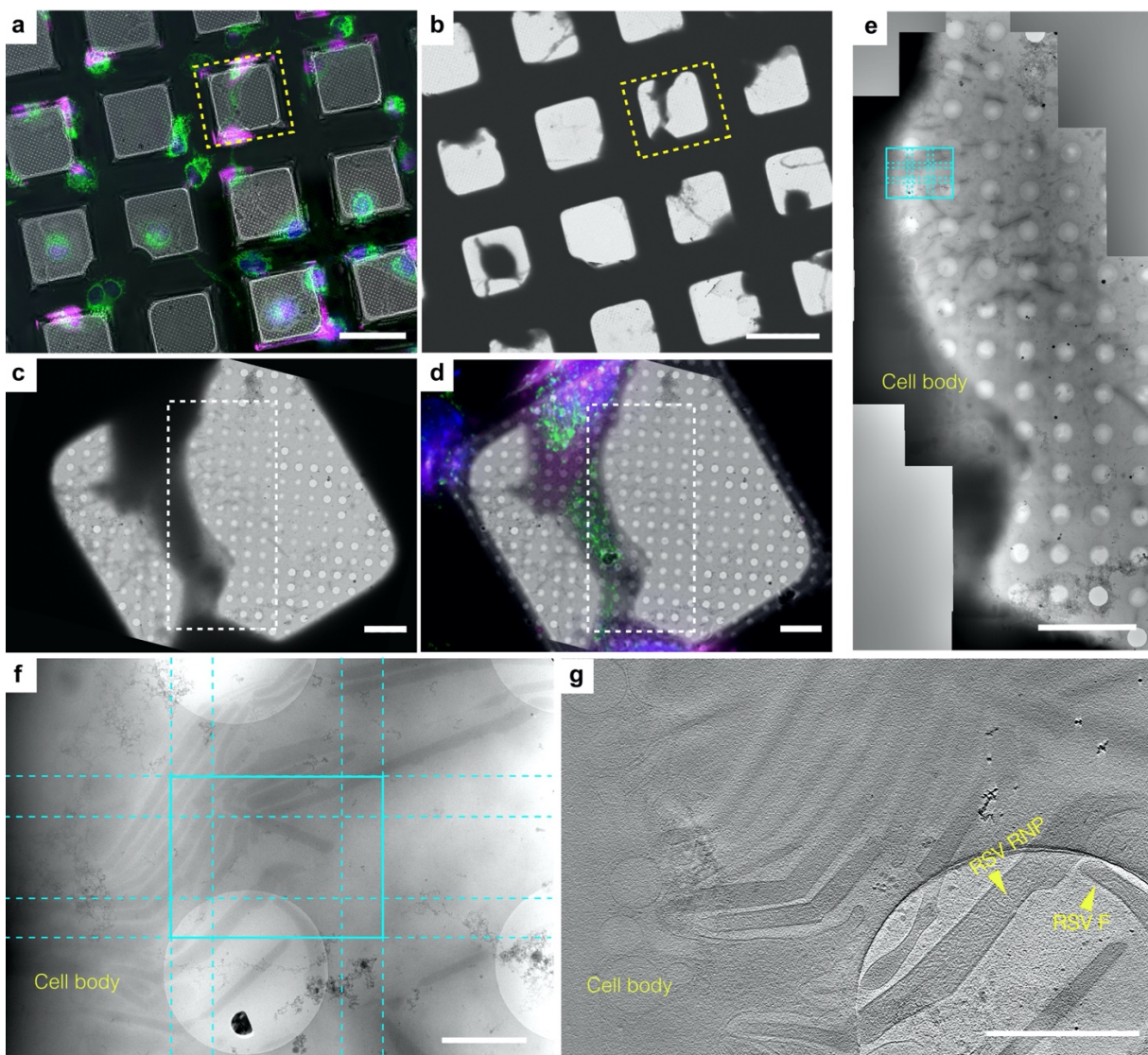
829
830
831 **Supplementary Figure 6. Large field of view of budding RSV virions captured by a**
832 **correlative cryo-FLM montage cryo-ET workflow.** Cryo-FLM **(a)** and cryo-EM **(b)** grid image
833 montages of RSV-infected HeLa cells (magenta) grown on a SiO$_2$ filmed R2/2 gold-mesh grid.
834 Mitochondria (green) and nucleus (blue) are labeled. Square of interest highlighted in yellow.
835 Scale bars, 100 μm. **c.** Magnified cryo-EM view of the yellow square in **(b)**. **d.** On-the-fly
836 CorRelator-based cryo-FLM and cryo-EM 2D correlation (yellow square in **a**, **b**) for the ROI
837 identification where montage tilt series were collected in SerialEM. Scale bars, 10 μm. **e.**
838 Magnified cryo-EM image montage of the white boxed area in **(d)**. A 3X3 tiling for montage cryo-
839 ET at the ROI (cyan tile pattern) where mitochondrion accumulate and RSV actively bud from the
840 cell plasma membrane. Scale bars, 10 μm. **f.** Montage cryo-ET tiles at 0° tilt (cyan, 6.8 x 5.3 μm
841 at pixel size of 4.603 Å). Scale bar, 1 μm. **g.** Tomographic slice, ~20 nm thick, through the 3X3
842 montaged tomogram (cyan ROI in **e**, **f**). RSV particles with clearly resolved fusion F glycoproteins
843 and ribonucleoprotein (RNP) complexes are present at budding sites along the cell body. Scale
844 bar, 1 μm.
845
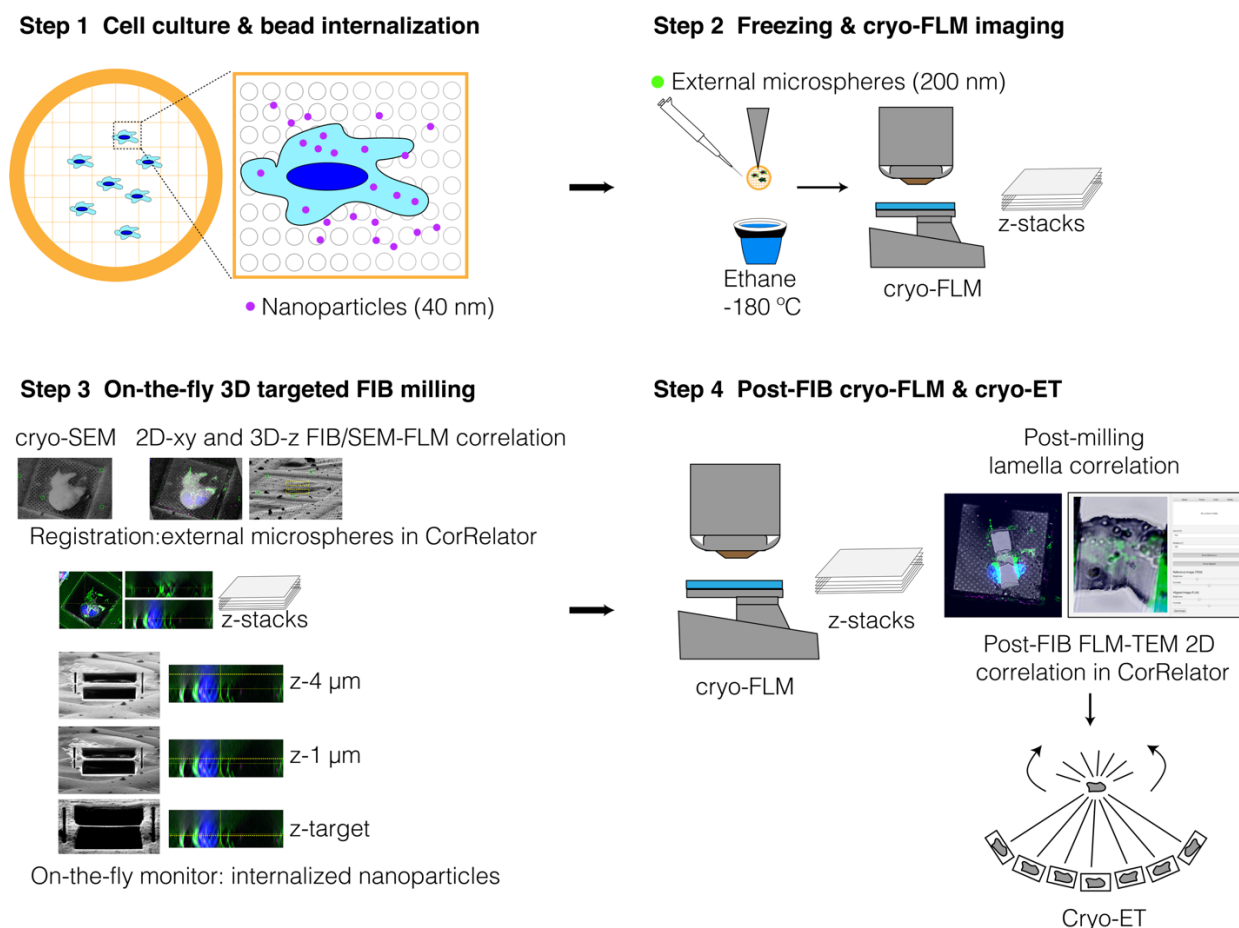
Supplementary Figure 7. Correlative 3D cryo-FLM-FIB-ET workflow. Overview of the correlative 3D cryo-FLM-FIB-ET workflow using two fiducial markers: 200 nm external fluorescent microspheres for coarse alignment and registration and cell-internalized 40 nm nanoparticles for on-the-fly 3D correlation during cryo-FIB milling. **Step 1.** Fluorescent nanoparticles (40 nm, pink) incubated with cultured cells were internalized. **Step 2.** Fluorescent microspheres (200 nm) were added prior to plunge freezing and grids were then imaged under a cryo-FLM system to acquire Z-stacks of regions of interest (ROIs). **Step 3.** The same grid was loaded onto and imaged with a dual-beam cryo-FIB-SEM system. Using the 3DCT Toolkit and CorRelator, cryo-FLM Z-stacks and 2D cryo-SEM and cryo-FIB images of ROIs were correlated for milling using 200-nm microspheres (FIB view, green circles) in X, Y, and Z. The placement of the milling boxes was refined based on the relative positions of the nanoparticles (pink) and signal of interest (green). **Step 4.** The same FIB-milled lamella was returned to the cryo-FLM system to acquire a new Z-stack cryo-FLM images for post-FIB-milling correlation. The lamella was then loaded into a cryo-TEM system. CorRelator-directed correlation between cryo-FLM and TEM images of the lamella was performed, and montage or regular tilt series were collected with SerialEM.
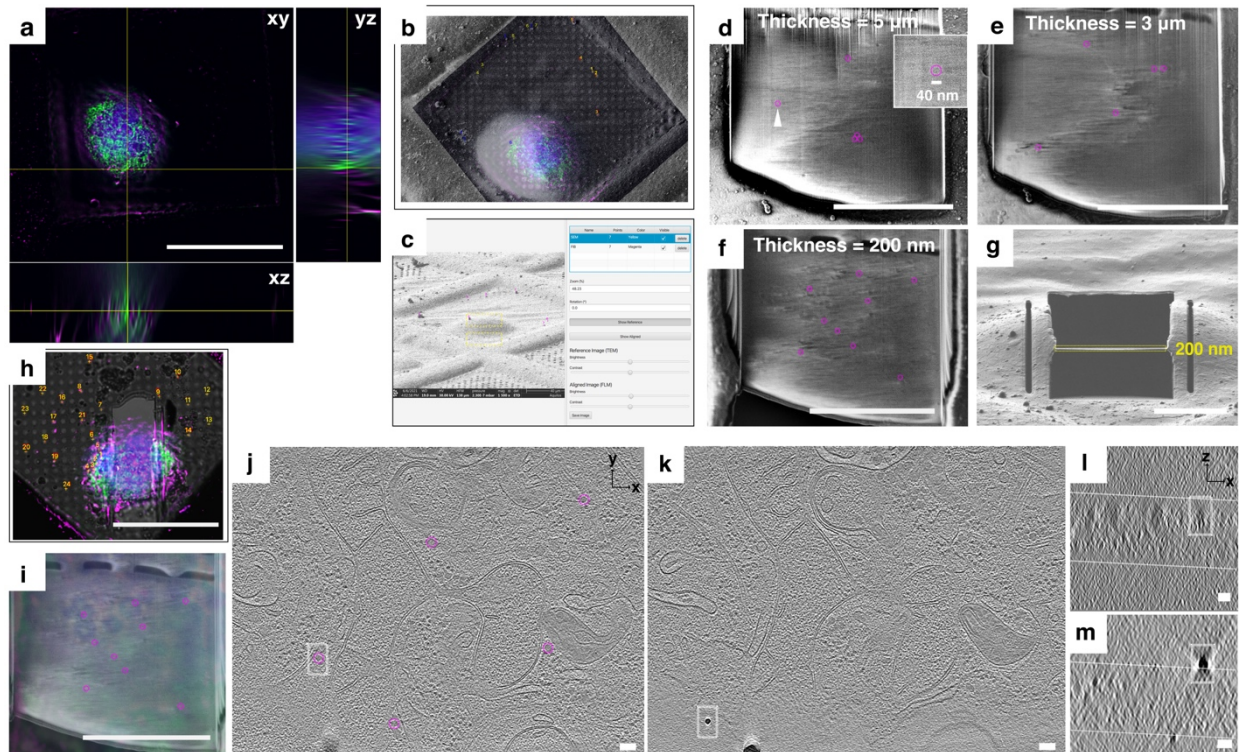
867
868
869 **Supplementary Figure 8. 3D correlation using internalized low-toxic fluorescent beads as**
870 **fiducial markers in cryo-FIB-SEM. a.** Orthogonal merged deconvoluted fluorescent cryo-FLM
871 (NA = 0.96) projections of labeled mitochondria (green), nucleus (blue), and internalized
872 nanoparticle (pink) inside the HeLa cell. Scale bar, 100 μm. **b-h.** On-the-fly 3D targeted FIB-milling
873 delineated in the Step 3 in Supplementary Figure 6. The X-Y plane correlation is done in
874 CorRelator **(b)** and initial X-Z correlation to position milling boxes in Z (yellow boxes) done in
875 3DCT and CorRelator **(c)**. Nanoparticle intensity visible under cryo-SEM as the lamella milling
876 progresses from a thickness of 5 μm **(d)** to 3 μm **(e)**, to the final 200 nm **(f, g)**, highlighted by pink
877 circles (40 nm in diameter). A representative nanoparticle in **(d)** was pointed out by white triangle
878 and enlarged in the inset. **h-i.** 3D cryo-FLM post-correlation of the post-FIB lamella and pre-FIB
879 corresponding fluorescent section in CorRelator. The corresponding nanoparticles in **(f)** are
880 highlighted in pink circles. Scale bars, 10 μm in **(d-g)** and **(i)**, 50 μm in **(h)**. Red and yellow
881 numbers in the GUI screenshots of **(b, c, h)** are registration points used in CorRelator. **j-m.**
882 Representative X-Y tomographic slices (thickness of 20 nm, pixel size of 4.603 Å) displaying the
883 nanoparticles (pink circle, **j**) and similar sized non-nanoparticle intensity (white boxed, **k**), and
884 their corresponding X-Z projections **(l-m)** of white boxed area in **(j)** and **(k)**. The tomogram Z-
885 volume boundaries are indicated by white dashed lines in **(l-m)**. Scale bars, 50 nm in **(j-m)**.
886 Nanoparticles are less electron dense than ice particles or regular gold fiducials.
887

888

889

890

891

892
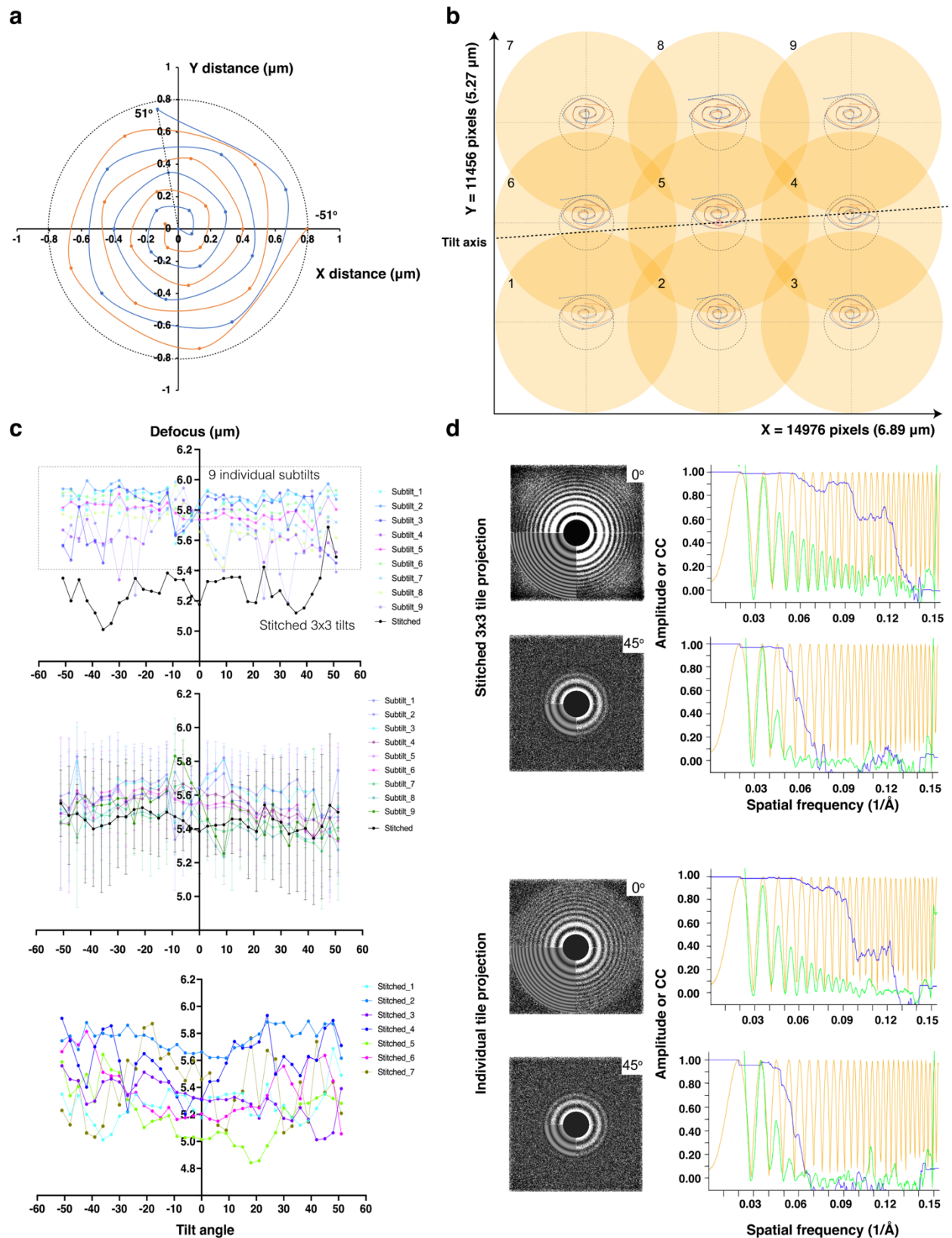
893   **Supplementary Figure 9. Defocus determination and CTF estimation of full stitched**
894   **montage and individual tile tilt series. a.** Benchmark spiral translation pattern applied to
895   distribute electron dose. To introduce global translation offsets, the central tile of the montage
896   follows spiral paths shifting outwards over the full course of the tilt series from -51° (orange points)
897   to 51° (blue points) in a dose-symmetric, three-degree increment and group of 3 scheme. The
898   translation maximum is 0.8 μm (black dotted circle, A_{final} = 1.5, Period = 3, Revolution = 15 as
899   spiral shape parameters). **b.** Cross-correlation alignment of cosine-stretched image shifts at each
900   tilt angle relative to 0° tilt in individual tile tilt series of the regular 3X3 montage pattern, using
901   Tiltxcorr in IMOD. The image shift between each tilt follows a stretched spiral along the X axis
902   when the optional scaling parameter of the translation is not applied. The image shifts of individual
903   tile tilt series were overall within the maximum distance of 0.8 μm (black dotted circle). Numbers
904   indicate the individual tile positions applied to both **(c)** and **(d)**. **c.** Defocus values of nine individual
905   tile sub-tilt series and the corresponding stitched 3X3 montage tilt series (pixel size of 4.603 Å),
906   following the same global spiral shift in **(a, b)** were estimated using CTFPLOTTER in IMOD: one
907   representative 3X3 stitched montage and nine individual tile tilt series (top), median variation at
908   each tilt angle over multiple 3X3 montage and corresponding tile tilt series (n = 3, middle), and 7
909   stitched montage tilt series (bottom) are shown. A target defocus of -5 μm was applied by
910   performing autofocusing prior to the tile collection at each tilt angle, along the tilt axis, 7.5 μm
911   away from the center of the montage tile to account for the size of the montage (6.89 x 5.27 μm)
912   and additional translation shift (0.8 μm). **d.** CTF estimation in CTFFIND4 by the 2D power spectra
913   (left) from projections at 0°, 45°, and -45° from a representative 3X3 stitched montage tilt series
914   and one of the individual tile tilt series (tile position 2 in **b**), and corresponding fitted 1D models
915   (right) showing radially averaged amplitude spectrum (green), CTF fit (orange), and CTF fit score
916   (blue).

917
918
919
920
921
922
923
924
925

926

927

928

929

930

931

932

933
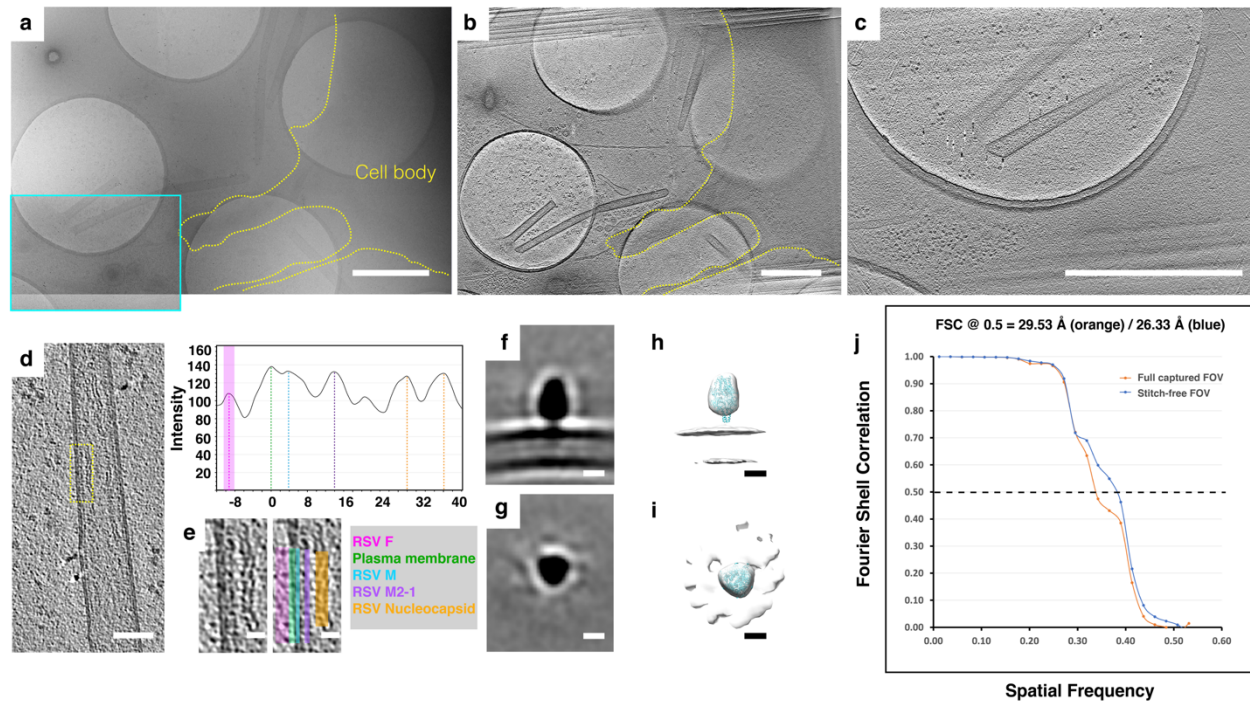
934
935
936 **Supplementary Figure 10. Sub-tomogram averaging of individual tile tomograms. a.** 3X3
937 montage cryo-ET image tiles at 0° tilt of RSV-infected BEAS-2B cells. The cell boundary is
938 delineated in yellow and one tile with viruses used for sub-tomogram averaging is highlighted in
939 cyan. **b.** Central slice of the stitched 3X3 montage tomogram in **(a)**, cell boundary (yellow). **c.**
940 Central ~18 nm slice of the reconstructed tomogram (pixel size of 9.206 Å) of the tile highlighted
941 in (**a**, cyan box). Scale bars, 1 μm in **a-c. d.** Reoriented Z-projection (9 nm thick) of the virion from
942 the tomogram in **(c)**. **e.** An enlarged view of virus (yellow dashed box in **d**) with virion components
943 noted in different colors and a linear density profile across the virion region. Scale bars, 100 nm
944 in **(d)**, 20 nm in **(e)**. **f-i.** Sub-tomogram averages of RSV F from individual tile tomograms collected
945 through the 3X3 montage cryo-ET workflow. The particles in overlapped stitched zones (15% in
946 X and 10% in Y) were excluded. **f-g.** Slices from a sub-tomogram average of binned 2 individual
947 tile tomograms (pixel size of 9.206 Å) of RSV F filtered to 27 Å in the side (**f**) and top (**g**) views.
948 **h-i.** RSV pre-fusion trimer model (PDB: 4JHW, cyan) fit into an isosurface of the sub-tomogram
949 average of F. Scale bars, 5 nm. **j.** FSC curves for sub-tomogram averages of F particles picked
950 from full captured field of view (orange, C3 symmetry expansion, n = 23250) and field of view free
951 from stitching overlaps (blue, C3 symmetry expansion, n = 20707) as stitch-free particles in sub-
952 tilt tomograms.
953

954

	Position 1 (x/y, 38/101)	Position 2 (x/y, 45/87)	Position 3 (x/y, 59/103)	Position 4 (x/y, 58/87)
No translation (a)	39.2 ± 5.2	85.1 ± 18.1	64.5 ± 7.7	105.1 ± 18.5
No translation lower dose by 30% (b)	27.5 ± 3.6	59.6 ± 12.5	45.2 ± 5.3	73.6 ± 12.9
Translation (c)	45.5 ± 3.2	77.1 ± 4.8	56.8 ± 7.4	79.2 ± 10.1
Translation lower dose by 30% (d)	31.8 ± 2.2	48.2 ± 3.3	39.8 ± 5.2	56.1 ± 7.1
Translation with x-axial correction (e)	45.2 ± 4.8	83.7 ± 10.8	66.7 ± 7.6	94.7 ± 10.8
Translation with x-axial correction lower dose by 30% (f)	31.7 ± 3.4	51.2 ± 7.6	46.7 ± 5.3	66.3 ± 7.5

955

Supplementary Table 1. Dose accumulation in $e^-/\text{Å}^2$/voxel at specified voxels in four sampling areas (radius of 10 x 10 x 1 voxel^2 pivoting around the central sampling points 1 to 4, X and Y voxel positions specified, indicated in **Supplementary Fig. 4**) of six different collection schemes with the same 3X3 montage tile pattern using *TomoGrapher* simulation. The mean and standard deviation were calculated. The Tilt Strategy parameters is also specified in Supplementary Fig. 4 (3X3 tile pattern, pixel size of 4.603 Å, beam size of 3.1 μm, from -51° to 51° tilts with a 3° increment, 1 or 0.7 $e^-/\text{Å}^2$ per tile per tilt).

963